Photocurrent Generation from Visible Light Irradiation of Covalent Polyoxometalate-Porphyrin Copolymers

Zhaohui Huo, Yiming Liang, Shu Yang, Dejin Zang, Rana Farha, Michel Goldmann, Hualong Xu, Antoine Bonnefont, Edoardo Matricardi, Guillaume Izzet, et al.

Photocurrent Generation from Visible Light Irradiation of Covalent Polyoxometalate-Porphyrin Copolymers

Zhaohui Huo, [a,b] Yiming Liang, [b] Shu Yang, [b] Dejin Zang, [b] Rana Farha, [c,d] Michel Goldmann, [c,e] Hualong Xu, [f] Bonnefont Antoine, [b] Edoardo Matricardi,[g] Guillaume Izzet, *[g] Anna Proust, [g] and Laurent Ruhlmann, *[b]

[a]Department of Chemistry, Guangdong University of Education, Guangzhou, 510303, People's Republic of China
[b]Université de Strasbourg, Institut de Chimie, UMR CNRS 7177, Laboratoire d'Electrochimie et de Chimie Physique du Corps Solide, 4 rue Blaise Pascal, CS 90032, 67081 Strasbourg cedex, France. E-mail: lruhlmann@unistra.fr
[c]Institut des NanoSciences de Paris, UMR CNRS 7588, Université Paris 6, 4 place Jussieu, boîte courrier 840, F - 75252 Paris, France
[d] LICORNE-ECE Paris Ecole d'Ingénieurs, 37 Quai de Grenelle, F - 75015 Paris, France
[e] Université Paris Descartes, 45 rue des Saints Pères, F - 75006 Paris, France
[f]Department of Chemistry, Shanghai Key Laboratory of Molecular Catalysis and Innovative Materials and Laboratory of Advanced Materials, Fudan University, Shanghai 200433, People's Republic of China
[g] Sorbonne Universités, UPMC Univ Paris 06, CNRS UMR 8232, Institut Parisien de Chimie Moléculaire, Université Pierre et Marie Curie, 4 place Jussieu, Case 42, 75252, Paris Cedex 05, France. E-mail: guillaume.izzet@sorbonne-universite.fr

* Corresponding authors. E-mail address: lruhlmann@unistra.fr (L. Ruhlmann) and guillaume.izzet@sorbonne-universite.fr (G. Izzet).

Abstract:

Four hybrid polyoxometalate–porphyrin copolymer films were obtained by the electrooxidation of zinc-*β*-octaethylporphyrin (**ZnOEP**) or 5,15-ditolylporphyrin (**H_2T_2P**) in the presence of organosilyl functionalized Keggin-type POMs $TBA_3[PW_{11}Si_2O_{40}C_{26}H_{16}N_2]$ (abbreviated **Py-$PW_{11}Si_2$-Py**) and Dawson-type POMs $TBA_6[P_2W_{17}Si_2O_{62}C_{26}H_{16}N_2]$ (abbreviated **Py-$P_2W_{17}Si_2$-Py**) bearing two remote pyridyl groups. The electropolymerization process of the four copolymers was monitored by EQCM.

The obtained copolymers were characterized by UV/Vis spectroscopy, X-ray photoelectron spectroscopy, electrochemistry, and AFM. Their impedance properties (EIS) were studied and their photovoltaic performances were also investigated by photocurrent transient measurements under visible light irradiation. These studies showed a correlation between impedance and photovoltaic performances, the films based on Dawson type POMs and Zn porphyrins giving the best results. This last system displayed one of the best photocurrent efficiency for a reported POM photosensitized hybrid.

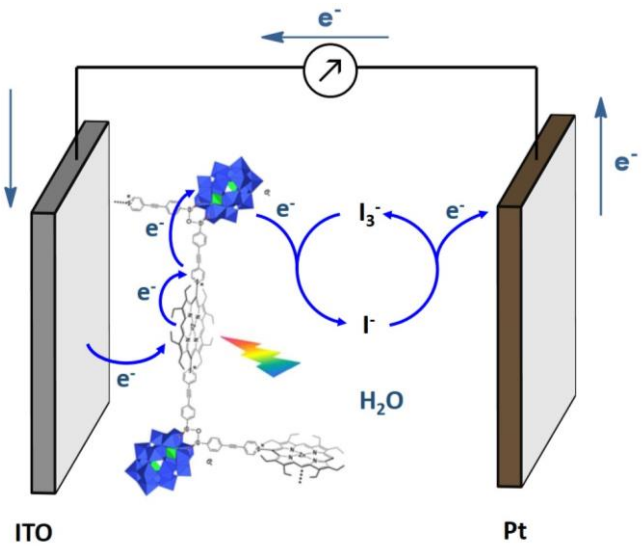

Keywords: copolymerization · organic–inorganic hybrid composites · polyoxometalates · porphyrinoids · thin films · photocurrent generation

1. Introduction

Polyoxometalates (POMs) form a unique class of inorganic metal–oxygen cluster compounds with applications in analytics, medicine, catalysis, electro- and photocatalysis, electronics, and material science **[1]**. POMs are negatively charged electron acceptors that can undergo multi-electron redox processes without decomposition, which are the basis for numerous catalytic processes **[1]**. In most cases POMs reach excited states only under UV irradiation (O → M LMCT absorption band) **[2]**, which strongly limits the use of POMs in solar visible light conversion materials. To expand the practical applications, their association to a visible-light photosensitizer via non-covalent, coordination or covalent bonding is thus a prerequisite.

Because of better process ability, covalent POM–porphyrin polymers would be better suited for building functional devices with photovoltaic properties **[3]**. To the best of our knowledge, there is only few examples of such an approach. Peng *et al.* reported copolymers with a conjugated photoactive organic skeleton **[4]** and hexamolybdate clusters embedded into the main-chain or as side-chain pendants **[5-6]**. These polymeric hybrids possessed intense visible absorption, however without fluorescence emission, indicating efficient fluorescence quenching by the incorporated POMs. The polymer was used as a component of a single-layer photovoltaic device (indium tin oxide (ITO)/polymer/Ca configuration), which exhibited a power conversion efficiency (PCE) of 0.15% **[5b]**. More recently, Peng *et al.* reported new organic–inorganic hybrid conjugated copolymers containing different amounts of hexamolybdate clusters covalently embedded in the main chain with imide-functionalized naphthodithiophene and 3,30-didodecyloxy bithiophene units showing PCEs up to 0.31% **[6b]**. The photovoltaic performance of this two materials are already very promising even if some improvements are needed for application. Moreover, several other covalently-linked POM–polymer hybrids have been reported, but the study of the photovoltaic properties of the materials has not been done yet **[7]**.

Even though the outcomes or efficiencies of these hybrid materials have not reached yet a sufficient level, the original designs and originality to synthesis innovative materials are still more than inspiring. Given this outcome, the scarcity of POM-based polymers for photocurrent generation, and our ongoing interest in photocatalysis by POM–porphyrin polymer conjugates under visible-light **[8]** irradiation, we decided to evaluate the efficiency of copolymers obtained from porphyrins and dipyridyl-substituted POMs for photocurrent generation. Recently, we reported the formation via a novel and original electropolymerization process, of mixed POM–porphyrin copolymer films with porphyrin and

either an Anderson-type POM $[MnMo_6O_{18}\{(OCH_2)_3CNHCO(4\text{-}C_5H_4N)\}_2]^{3-}$ **[8]** organic derivatives of the Dawson $[P_2W_{15}V_3O_{62}]^{9-}$ [**9**] or the Linqvist $[V_6O_{13}\{(OCH_2)_3CNHCO(4\text{-}C_5H_4N)\}_2]^{2-}$ **[10]** type POMs bearing pyridyl ligands. Some of them displayed interesting photocatalytic properties under visible light illumination **[8]**. Therefore, we believe that it would be of great interest to form new covalent POM–porphyrin copolymers by varying the type of POMs, and to study the role of the POMs in the polymer backbone.

In the present paper, we report the electropolymerization of **ZnOEP** in the presence of the silyl derivatized Keggin- and Wells-Dawson POM-based platforms that were functionalized with pyridyl groups **[11-12]**. Organosilyl functionalized Keggin-type POMs $TBA_3[PW_{11}Si_2O_{40}C_{26}H_{16}N_2]$ **[13]** (abbreviated **Py-PW$_{11}$Si$_2$-Py**) and Dawson-type POMs $TBA_6[P_2W_{17}Si_2O_{62}C_{26}H_{16}N_2]$ **[14]** (abbreviated **Py-P$_2$W$_{17}$Si$_2$-Py**) bearing two pyridyl groups were synthetized and were used for electrochemical preparation of the copolymers with porphyrin (**ZnOEP** and **H$_2$T$_2$P**) using the previously reported $E_1(E_{2+n}C_{Nmeso}E_{3+n}C_B)_nE_{4+n}$ process (TBA= tetrabutylammonium) **[15-17]**.

We herein describe the electropolymerization and the characterization of the four hybrids copolymers obtained from organo-Keggin or organo-Dawson type POM bearing two pyridyl groups, **Py-PW$_{11}$Si$_2$-Py** or **Py-P$_2$W$_{17}$Si$_2$-Py** and the molecular precursor porphyrin zinc-*β*-octaethylporphyrin (**ZnOEP**) or 5,15-ditolylporphyrin (**H$_2$T$_2$P**) (Scheme 1). The copolymers have been characterized by UV–vis spectroscopy, X-Ray Photoelectron spectra (XPS), Atomic Force Micrographs (AFM), EQCM, and electrochemistry. We also report their photocurrent response under visible light irradiation.

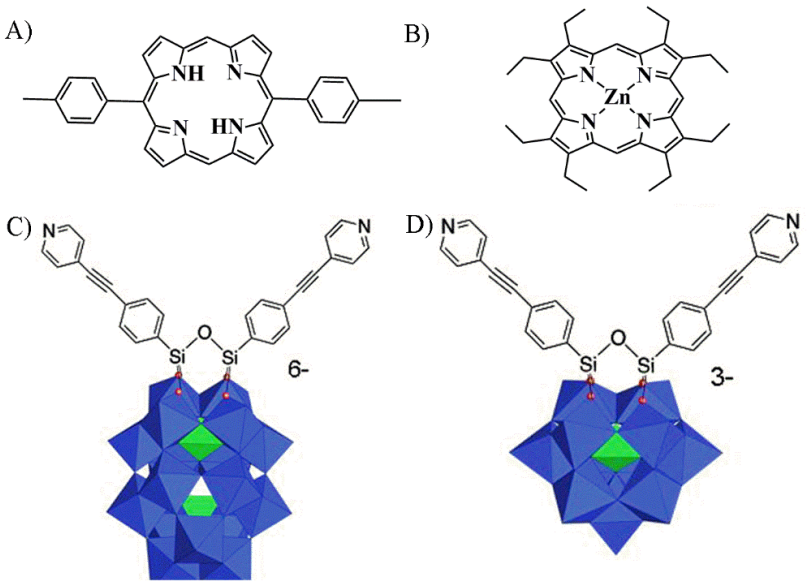

Scheme 1. Representation of A) **H_2T_2P**, B) **ZnOEP**, C) Dawson type POM $TBA_6[P_2W_{17}Si_2O_{62}C_{26}H_{16}N_2]$ (abbreviated **Py-$P_2W_{17}Si_2$-Py**), and D) Keggin type POM $TBA_3[PW_{11}Si_2O_{40}C_{26}H_{16}N_2]$ (abbreviated **Py-$PW_{11}Si_2$-Py**).

2. Experimental

2.1 Reagents and apparatus

All solvents were of reagent grade quality and used without further purification. The zinc-β-octaethylporphyrin (**ZnOEP**) was purchased from Sigma-Aldrich, and The 5,15-ditolylporphyrin (**H_2T_2P**) was purchased from SAS PorphyChem®. Keggin-type polyoxovanadate $[PW_{11}Si_2O_{40}C_{26}H_{16}N_2]$ TBA_3 (abbreviated **Py-$PW_{11}Si_2$-Py**) and Dawson-type polyoxovanadate $[P_2W_{17}Si_2O_{62}C_{26}H_{16}N_2]$ TBA_6 (abbreviated **Py-$P_2W_{17}Si_2$-Py**) were synthesized following the reported synthetic procedures [**18-19].**

Voltammetric data have been recorded with a standard three-electrode system using a PARSTAT 2273 potentiostat. The electrolyte was $CH_3CN/1,2\text{-}C_2H_4Cl_2$ (3/7) containing 0.1 mol L^{-1} of tetrabutylammoniumhexafluorophosphate (NBu_4PF_6). Single-side coated indium-tin-oxide (ITO, SOLEMS, 25–35 Ω/cm^2) electrodes with a surface area of 1 cm^2 were used as working electrode, and a platinum wire as auxiliary electrode. The reference electrode was the saturated calomel electrode which was electrically connected to the solution by a junction bridge filled with electrolyte. The electrochemical impedance spectrum (EIS) measurements were carried out at sinusoidal voltage

excitation with amplitude of 10 mV in a frequency range from 100 kHz to 100 mHz. The ITO electrodes were also used to obtain UV–vis spectra of the electrochemically deposited copolymers on an Agilent 8453 spectrophotometer.

A QCA-922 (SEIKO EG&G instrument) system combined with Versa STAT 3 was used for simultaneous electrochemical quartz crystal measurement (EQCM) and cyclic voltammetric measurements. The electrochemical cell was assembled in a glove box using an ITO AT-cut quartz crystal resonator (mirror finished, resonant frequency: 9.08 MHz ± 50 kHz, A = 0.2 cm^2, SEIKO EG&G., LTD) as working electrode, a platinum wire as counter electrode, and a Ag/AgCl wire as a quasi-reference electrode. The solution used for the electropolymerization here is the same as the one we used for electropolymerization of the copolymers with the larger ITO electrode. Iterative scans were conducted at a scan rate of 100$mV \cdot s^{-1}$ at room temperature with simultaneous recording of the quartz resonance frequency. The change of the quartz resonance frequency (Δf) was converted into the mass change (Δm) on the ITO-coated quartz during iterative cycling by applying Sauerbrey's equation (eq 1):

$$\Delta f = -2f_0^2 \Delta m / A(\mu.\rho)^{1/2} \qquad (1)$$

where f_0 is the resonant frequency of the fundamental mode, ρ is density of the crystal (2.684g/cm^3), A is working area (0.2 cm^2) of the ITO quartz crystal resonator, μ is shear modulus of quartz ($2.947\times10^{11} g \cdot cm^{-1} \cdot s^{-2}$).

XPS experiments were carried out on a RBD upgraded PHI-5000C ESCA system (Perkin-Elmer) with MgKR radiation (*h*=1253.6 eV) or Al KR radiation (*h*= 1486.6 eV). In general, the X-ray anode was run at 250W and the high voltage was kept at 14.0 kV with a detection angle at 54°. The pass energy was fixed at 23.5, 46.95, or 93.90 eV to ensure sufficient resolution and sensitivity. The base pressure of the analyzer chamber was about 5×10^{-8} Pa. The sample was directly pressed to a self-supported disk (10 x 10 mm) and mounted on a sample holder then transferred into the analyzer chamber. The whole spectra (0-1100 eV) and the narrow spectra of all the elements with higher resolution were both recorded by using RBD 147 interface (RBD Enterprises, U.S.A.) through the Auger Scan 3.21 software. Binding energies were calibrated by using the containment carbon (C1s = 284.6 eV). The data analysis was carried out by using the RBD Auger Scan 3.21 software provided by RBD Enterprises or XPS Peak 4.1 provided by Raymund W.M. Kwok (The Chinese University of Hongkong, China).

Atomic force micrographs (AFM) measurements have been conducted directly on the ITO surfaces using a Dimension 3100 (Veeco) in the tapping mode under ambient conditions. Silicon cantilevers (Veeco probes) with a spring constant of 300 N/m and a resonance frequency in the range of 120–139 kHz have been used. The scanning rate was 1.0 Hz.

Photoelectrochemical responses for films on ITO were obtained by on-off light illumination of a 300 W Xe arc lamp (with $\lambda = 385$ nm long pass filter) in acetonitrile containing I_2 5 mmol L^{-1} and NaI 0.5 mol L^{-1} with two-electrode system. I_3^- and I^- anions act as redox mediator and also as electrolyte in order to improve the conductivity and thus increase the current magnitude.

Please note that the measurements are performed using two electrodes.

3. Results and Discussion

3.1 Redox behavior of the two organo-POM monomers

The redox behaviour of **Py-$PW_{11}Si_2$-Py** and **Py-$P_2W_{17}Si_2$-Py** showed three and four successive reduction processes respectively attributed to the W^{VI}/W^{V} couples (Fig. 1) using glassy carbon electrode, respectively at -0.34 V, -0.87 V, and -1.50 V *vs.* SCE for **Py-$PW_{11}Si_2$-Py** and at -0.57 V, -0.94 V, -1.45 V, and -1.73 V *vs.* SCE for **Py-$P_2W_{17}Si_2$-Py**, as expected **[11]**. The process observed at +0.4 V/ ECS corresponds to the oxidation of the ferrocene added as internal reference (external reference: SCE). The measured redox waves are the same in the presence and in the absence of ferrocene, confirming that the presence of ferrocene is not affecting the redox behaviour of the organo-POMs monomers (Fig. S13). In the case of **Py-$PW_{11}Si_2$-Py**, the redox process showed similar behaviors using glassy carbon and ITO electrodes (Fig. 1, black curve). However, for **Py-$P_2W_{17}Si_2$-Py**, ill-defined waves were observed when using a ITO electrode (Fig. 1B, red curve). This may be due to the negative charge of Dawson **Py-$P_2W_{17}Si_2$-Py** and then to the electrostatic repulsion between the surface of the working electrode under cathodic polarization and **Py-$P_2W_{17}Si_2$-Py** bearing six negative charges.

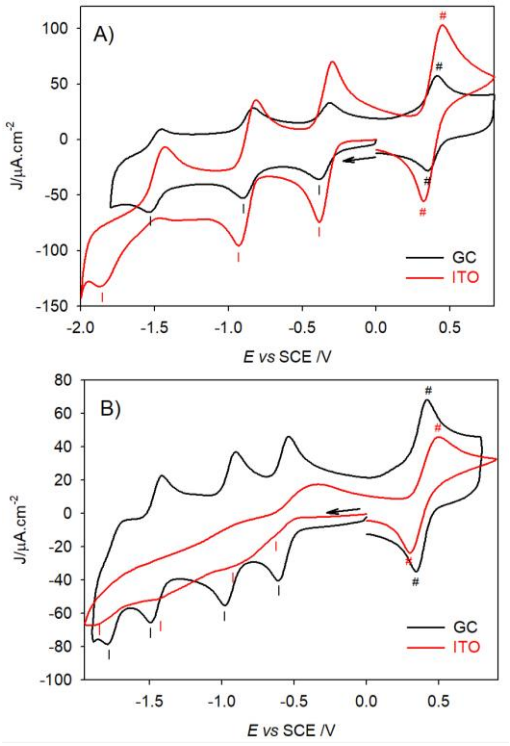

Figure 1. Cyclic voltammograms of 0.25 mmol L^{-1} A) $TBA_3[PW_{11}Si_2O_{40}C_{26}H_{16}N_2]$ and B) $TBA_6[P_2W_{17}Si_2O_{62}C_{26}H_{16}N_2]$ in CH_3CN in the presence of 0.1 mol L^{-1} $TBAPF_6$. Working electrode: ITO (S = 1.00 cm^2) and glassy carbon (GC), d = 6 mm (S = 0.28 cm^2). (←) Start of the scan. Scan rate: 0.1 V s^{-1}. Peak $^{\#}$: Fc/Fc^+ internal reference. Reference: SCE.

The cyclic voltammograms of **ZnOEP** and **H_2T_2P** showed typical redox behavior for porphyrin. For instance, **ZnOEP** showed two successive oxidation waves at 0.71 V and 1.08 V *vs.* SCE attributed to the generation of the π-radical cation **$ZnOEP^{+\bullet}$** and the dication **$ZnOEP^{2+}$** porphyrin respectively. The first reduction of the porphyrin giving the radical anion **$ZnOEP^{-\bullet}$** at -1.66 V vs. SCE was also measured. In the case of **H_2T_2P**, two successive reductions and two successive oxidation processes were measured at 1.01, 1.27, -1.20 and -1.66 V (Figs. 9-12, Table 1). It corresponds to the generation of the π-radical cation, dication, radical anion and dianion respectively.

3.2 Synthesis and characterization of the Poly-$PW_{11}Si_2$-porphyrin and Poly-$P_2W_{17}Si_2$-porphyrin copolymers

ITO electrodes, with a surface of 1 cm^2, were used as working electrodes. All of the electropolymerizations were carried out under the same experimental conditions by iterative potential scans in 0.1 mol L^{-1} solutions of tetrabutylammonium hexafluorophosphate (NBu_4PF_6) in 1,2-$C_2H_4Cl_2$/CH_3CN (7:3) containing 0.25 mmol.L^{-1} of the studied porphyrin zinc-*β*-octaethylporphyrin (**ZnOEP**) or 5,15-ditolylporphyrin (**H_2T_2P**) and the **Py-POM-Py** (**Py-$PW_{11}Si_2$-Py** or **Py-$P_2W_{17}Si_2$-Py)** under an argon atmosphere (Scheme 1). For each copolymer, the number of scans (n) involved in the iterative procedure was varied in order to modulate the thickness of the films. After electropolymerization, the modified working electrodes were washed with CH_3CN in order to remove the monomers and the conducting salt present on the deposited films.

The electrochemical synthesis of the POM porphyrin copolymers relies on the previously reported $E_1(E_{2+n}C_NE_{3+n}C_B)_nE_{4+n}$ process of nucleophilic substitution on porphyrins **[8,10]**.

First, the porphyrin radical cation (**$ZnOEP^{\bullet+}$**, electrochemical step E_1) and dication (**$ZnOEP^{2+}$**, electrochemical step E_2) are electrogenerated. Then, **$ZnOEP^{2+}$** can be attacked by a dipyridil group (abbreviated Py-POM-Py) (chemical step C_{Nmeso}) at *meso*-carbon position to yield an isoporphyrin. This later compound can be oxidized (electrochemical step E_3) and the hydrogen atom initially located on the *meso*-carbon is released inducing the rearomatisation of the porphyrin (chemical step C_B) which give the mono-substituted porphyrin **ZnOEP-*meso*-Py^+-POM-Py**. At this stage, monosubstituted porphyrin is obtained with one pyridinium covalently connected to the porphyrin and one pendant pyridyl group which is still active for nucleophilic attack. This pendant pyridyl group can further attack oxidized porphyrin continuing the growth of the copolymer.

The polarization of a working electrode at the porphyrin's second ring-oxidation potential in the presence of **Py-POM-Py**, leads to the formation of hybrid films $[POM\text{-}porphyrin]_n$ (Scheme 2).

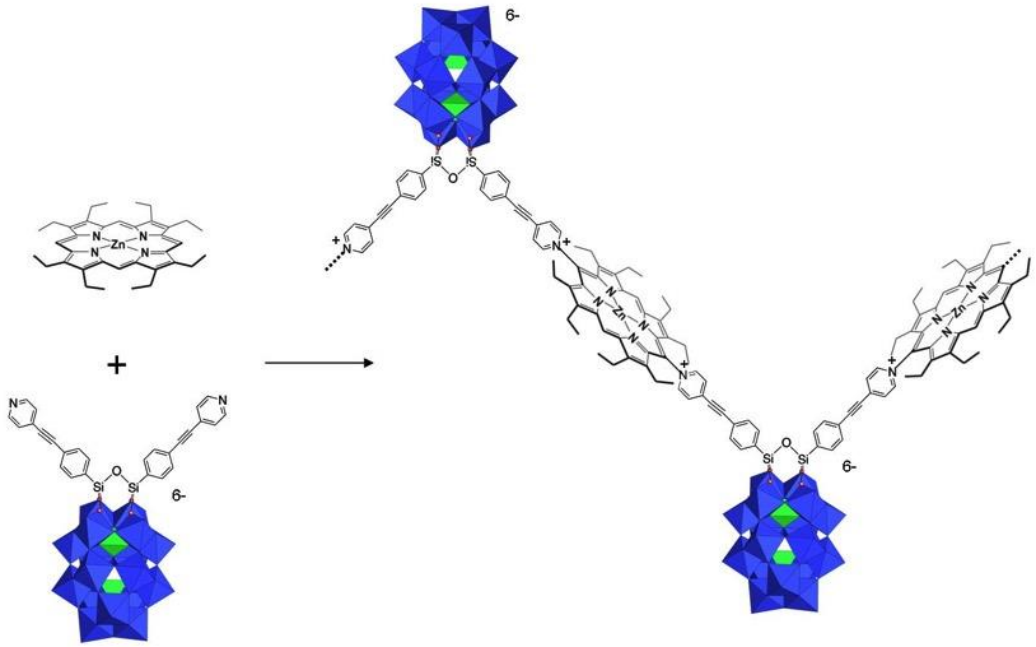

Scheme 2. Electropolymerization scheme of **ZnOEP** in the presence of **Py-$P_2W_{17}Si_2$-Py** ($TBA_6[P_2W_{17}Si_2O_{62}C_{26}H_{16}N_2]$).

The global reaction can be written as Equation (2), assuming that mainly the bisubstitution of the porphyrin is occurring:

(n+1) Porph + (n+1) **Py-POM-Py** -(4n+2) e^- → Porp-(**Py^+-POM-Py^+**-Porph)$_n$-**Py^+-POM-Py** + (2n+1) H^+ (2)

The reaction produced H^+ ions. Scanning the potential up to -1.2 V allowed the reduction of these protons into H_2 while they accumulated in solution when the scan range was limited between 0.0 to +1.6 V. In the both cases, they did not perturb the coating of the electrodes. UV-visible spectroscopy demonstrated that the demetallation of the metalloporphyrin **ZnOEP** or even the protonation of the free base porphyrin **H_2T_2P** did not occur in any cases. In the case of **ZnOEP** (Scheme 2), for which the four *meso* positions are substitutable (positions occupied by a proton atom), nucleophilic attack could occur at positions 5, 10, 15, or 20. As a result, in addition of the bi-substitution (in *meso* positions

5, 10 and 5, 15), tri-substitution or even tetra-substitution of the **ZnOEP** could *a priori* be formed leading to the formation of various branched forms of the copolymer. However, previous results have shown that mainly bisubstitution of the **ZnOEP** were kinetically observed (Scheme 2) **[8,10]**. In the case of the free base porphyrin **H_2T_2P** (Scheme 1), only positions 5 and 15 were available for substitution leading to the formation of linear 1D copolymers according to the above reaction (1).

Figure 2 illustrates the evolution of the CVs during the electropolymerization of **ZnOEP** in the presence of equimolar amounts of **Py-$PW_{11}Si_2$-Py**. During the first scan in reduction, two clear reduction peaks attributed to the POM units were detected at -0.34 V and -0.88 V *vs.* SCE (peaks a and c, Fig. 2B). In the second scan, an additional irreversible reduction peak appeared at ca. -0.77 V *vs.* SCE (peak b, Fig. 2B), which was assigned to the reduction of the pyridinium units of the dipyridinium-POM (-Py^+-POM-Py^+-) spacers of the on-growing polymer (ZnOEP-Py^+-POM-Py^+)$_n$ **[16-17]**. The irreversibility of the signal indicated that the generated pyridyl radicals were not stable and reacted further to give formation of C-C bound resulting from the coupling between two radical pyridyl. Indeed, the dimerization of pyridyl radicals when the 2-, 4- or 6-positions are free has often been discussed in the literature **[20-21]**. In our case, only 2- or 4-positions can react, the 6-positions being occupied **[21,22]**. During the electropolymerization, one other additional peak (noted with an asterisk) was observed and corresponded to the reduction of the isoporphyrin, an intermediate of reaction **[15,23]**. The intensity of peaks noted a and c increased with repetitive scans indicating the regular growth of the polymeric films at the electrode. A similar behavior was observed when *meso*-substituted porphyrin **H_2T_2P** was used instead of (Fig. S14 and Fig. S15B).

In the positive potential range for the first scan, three oxidation peaks (peaks d, e and f in Fig. 2B) were detected. The first and the second one-electron oxidation peaks (peaks d and e) were attributed

to the generation of the π-radical porphyrin cation and dication respectively, while the third peak (peak f) might be ascribed to the oxidation of the oligomer already formed. A similar redox behavior was also observed using **H_2T_2P** instead of **ZnOEP** (Fig. S14) but in this case only two irreversible signals were observed. The oxidation of **H_2T_2P** units also needed a higher positive potential, and the oxidation peaks merged when increasing the number of scans. In the case of the free base porphyrin **H_2T_2P,** it is noteworthy that protonation by the H^+ ions released by the electropolymerization was not detected. It suggests that the kinetic of the nucleophilic attack of **Py-$PW_{11}Si_2$-Py** with the oxidized porphyrin **$H_2T_2P^{2+}$** is probably faster than the proton abstraction of the dication free base porphyrin **$H_2T_2P^{2+}$** (reaction with the electrolyte or the solvent giving protonated porphyrin), which generally gives mono- or diprotonated porphyrin **[24]**. Furthermore, protonation of the one or two pendant pyridyl groups of **Py-POM-Py** subunits may probably have occurred, but protonated $^+$HPy-POM-PyH^+ and/or Py-POM-PyH^+ were still reactive with the dication porphyrin through their equilibria with the neutral form. Copolymers were also obtained by cyclic scanning (0.1 Vs^{-1}) in the potential range from 0 to +1.60 V *vs.* SCE. In this case, the obtained copolymers exhibited redox behavior similar to the one observed when scanning from -1.20 to +1.60 V *vs.* SCE (Fig. S15).

In the case of the organo-Dawson hybrid **Py-$P_2W_{17}Si_2$-Py**, the redox signal corresponding to the reduction of POM unit were harder to detect when using ITO as working electrode, even in the pure **Py-$P_2W_{17}Si_2$-Py** solution without porphyrin (see Fig. 1 of the section: Redox behavior of the two organo-POM monomers). From the second iterative scan in the presence of porphyrin, the signal reduction of the pyridinium appeared and the intensity of this peak increased as the iterative scan number increased between -1.00 V and +1.60 V *vs.* SCE (Fig. S16A and Fig. S16A'). This behavior can be explained by the merging of the peak with the second reduction of **Py-$P_2W_{17}Si_2$-Py** ($W^{VI/V}$

couple).

An additional wave could be observed near +0.5 V (Fig. S16B and Fig. S17B) during the formation of copolymer **poly-$P_2W_{17}Si_2$-H_2T_2P**. The origin of this additional wave is not clear at the present stage, but it can be attributed to the presence in solution of **H^+Py-$P_2W_{17}Si_2$-Py** and/or **H^+Py-$P_2W_{17}Si_2$-Py$^+$H** resulting to the acid-base reaction between **Py-$P_2W_{17}Si_2$-Py** and H^+ liberated during the substitution (equations 3-4):

$$HPy^+\text{-POM-Py} + e^- \rightarrow \text{Py-POM-Py} + 1/2H_2 \qquad (3)$$

$$HPy^+\text{-POM-}^+\text{PyH} + 2e^- \rightarrow \text{Py-POM-Py} + H_2 \qquad (4)$$

Another explanation is the formation of protonated porphyrin during its oxidation. In this case, formation of the protonated **$H_4T_2P^{2+}$** intermediate can occur either with the proton generated by the nucleophilic reaction (eq. 1) or via the reaction with the solvent or the electrolyte, even in strictly anhydrous conditions, as already evidenced **[24]**. Protonated porphyrin can in turn react, with **Py-POM-Py** to exchange the proton(s) leading to the formation of the large quantity of Py-POM-PyH^+ and/or HPy^+-POM-PyH^+, which were detected during the electropolymerization. Other explanation could be the protonation of the Dawson type POM that might induce the anodic shift of the first reduction due to the decrease of the global charge of the polyanion.

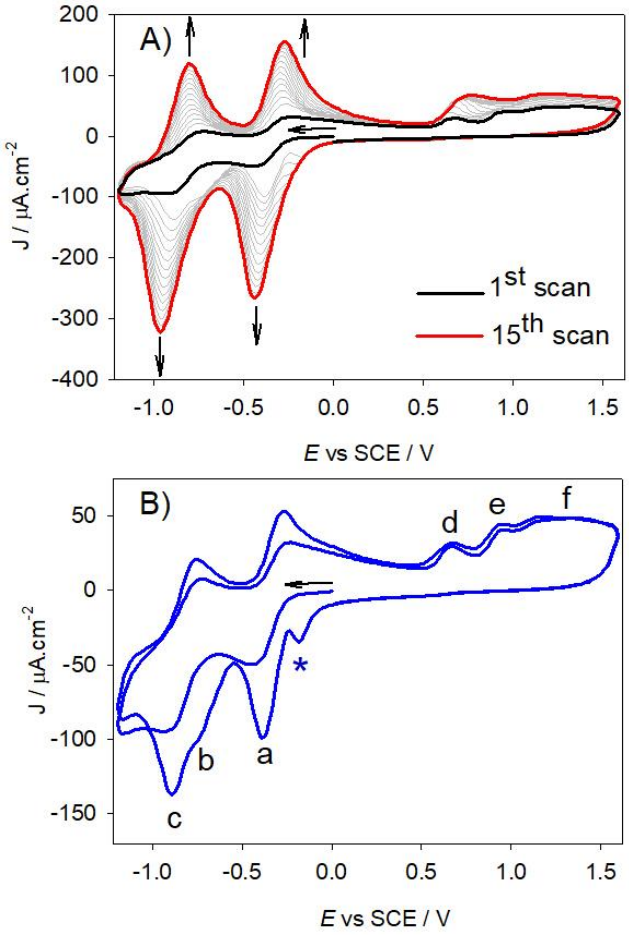

Figure 2. Cyclic voltammograms recorded between −1.20 V and +1.60 V *vs.* SCE during the electropolymerization of 0.25 mmol L^{-1} **ZnOEP** with 0.25 mmol L^{-1} **Py-$PW_{11}Si_2$-Py**, (A) first 15 scans and B) first 2 scans) in CH_3CN/1,2-$C_2H_4Cl_2$ (3/7) in the presence of 0.1 mol L^{-1} $TBAPF_6$. Working electrode: ITO. (←) Start of the scan. S =1 cm^2; scan rate: 0.1 V s^{-1}. Peak *: reduction of the isoporphyrin.

3.3 Electrochemical Quartz Crystal Microbalance (EQCM) for the copolymer deposition

The electropolymerization process was monitored by EQCM. Fig. 3 and Figs. S18-S20 show the simultaneously recorded mass changes Δm and cyclic voltammograms between 0.00 and +1.60 V with an ITO working electrode deposited on an AT-cut quartz crystal resonator, the quartz resonance frequency Δf decreased with each consecutive cycle, with a concomitant increase in the mass of the copolymer. By using the Sauerbrey's equation **[25]**, this change in mass was calculated.

Besides, the first scan in Figure 3 shows that a significant decrease of the frequency and consequently

increase of the mass is observed after the second oxidation peak revealing that i.e electropolymerization involves the formation of the dication porphyrin **ZnOEP^{2+}**.

The smooth drop in quartz resonance frequency and the simultaneous mass increase Δm showed continuous growth of the copolymer. The coverage after 25 iterative scans between 0 and +1.60 V was about 15.3, 15.7, 41.2 and 32.5 µg cm^{-2} for **poly-PW$_{11}$Si$_2$-ZnOEP**, **poly-PW$_{11}$Si$_2$-H$_2$T$_2$P**, **poly-P$_2$W$_{17}$Si$_2$-ZnOEP** and **poly-P$_2$W$_{17}$Si$_2$-H$_2$T$_2$P** copolymers, respectively.

The highest mass was obtained with the **poly-P$_2$W$_{17}$Si$_2$-ZnOEP** and **poly-P$_2$W$_{17}$Si$_2$-H$_2$T$_2$P** copolymers probably due to higher the molecular mass of Dawson type hybrid **Py-P$_2$W$_{17}$Si$_2$-Py** subunit (6046 g mol^{-1}) compared to that of **Py-PW$_{11}$Si$_2$-Py** subunit (3833 g mol^{-1}).

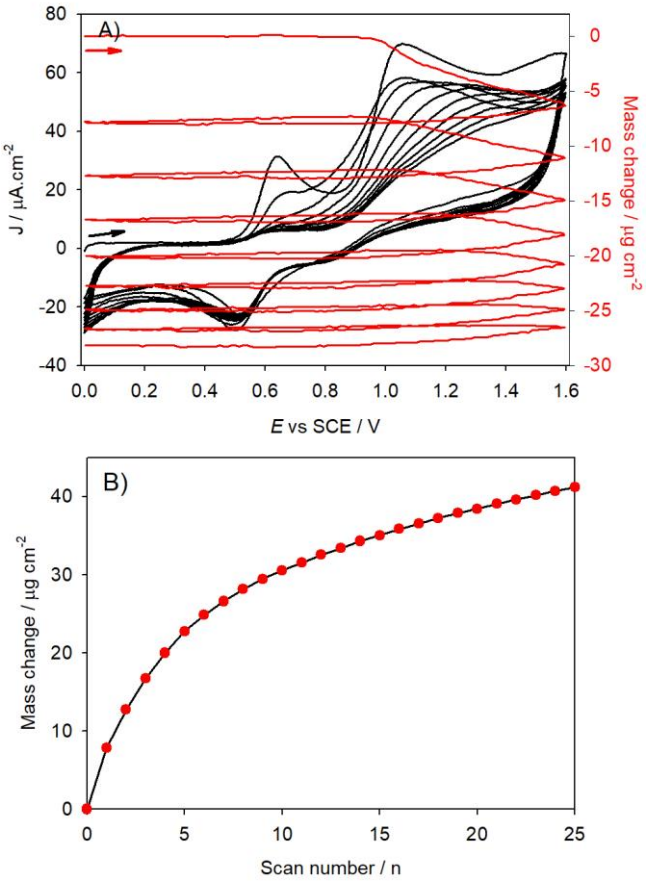

Figure 3. A) Consecutive cyclic voltammograms (first 10 scans) and EQCM measurements for the first 10 scans during the electropolymerization of 0.25 mmol L^{-1} **ZnOEP** with 0.25 mmol L^{-1} **Py-P$_2$W$_{17}$Si$_2$-Py** in CH_3CN/1,2-$C_2H_4Cl_2$ (3/7) in the presence of 0.1 mol L^{-1} $TBAPF_6$. Working electrode: ITO (S = 0.2 cm^2) deposited on a 9.08 MHz AT-cut quartz crystal. v = 100 mV s^{-1}. B) Mass change

(Δm) calculated versus the number of scan n.

Indeed, the mass difference between the copolymers is partly due to the different charges and then number of counter-cations: the charge of **Py-$P_2W_{17}Si_2$-Py** is 6- and 6 TBA counter-cations are needed to keep the electroneutrality of the copolymer while **Py-$PW_{11}Si_2$-Py** possesses only 3- and then 3 counter-cations TBA. The difference of mass deposited stems also from the molecular mass of the Dawson type POM ($TBA_6[P_2W_{17}Si_2O_{62}C_{26}H_{16}N_2]$, 6046,56 $g.mol^{-1}$) which is higher than for Keggin type POM $TBA_3[PW_{11}Si_2O_{40}C_{26}H_{16}N_2]$ (3833.17 $g.mol^{-1}$). A minor factor is also the lower molecular weight of **H_2T_2P** (490.60 $g.mol^{-1}$) than **ZnOEP** (598.14 $g.mol^{-1}$). It can also be explained by the number of *meso* positions available for the substitution: two for **H_2T_2P** *versus* four for **ZnOEP**.

The experimental copolymer mass deposited *per* charge unit can be determined by integrating the charge of the current-potential curves for the first 10 iterative scan giving 11.6 mg/C for **poly-$P_2W_{17}Si_2$-ZnOEP**, while the theoretical yield of the copolymer mass deposited *per* charge unit according to Figure 3 is equal to 18.0 mg/C (with one **Py-$P_2W_{17}Si_2$-Py** *per* **ZnOEP**) after 10 iterative scans between 0 and +1.6 V ($v = 100\ mV.s^{-1}$) leading to a faradic yield of 64 %. For **poly-$PW_{11}Si_2$-ZnOEP**, the faradic yield of 55 % (Fig. S18). In the case of **H_2T_2P- Py-$P_2W_{17}Si_2$-Py and of H_2T_2P-Py-$PW_{11}Si_2$-Py**, under similar conditions, the faradic yields are of 16 % and 25 % respectively.

These lower yields when free base **H_2T_2P** is used can be explained by the competitive reaction of protonation of the free base porphyrin during the oxidation of the porphyrin and the electropolymerization as discussed by Le Mest et al. **[26]**.

3.4 Cyclic voltammetric investigations of the films

The electrochemical behaviors of the four films were studied by cyclic voltammetry (Fig. 4, Figs. S21-S22 and Table 1).

For **poly-$PW_{11}Si_2$-H_2T_2P**, two well-defined reduction peaks (peak a and peak c in Fig. 4A) were attributed to the reduction of W^{VI} to W^{V} on the basis of the redox behaviour of the **Py-$PW_{11}Si_2$-Py**. Peak b corresponds to the irreversible pyridinium reduction, deduced from the cyclic voltammograms obtained during the electropolymerization (Fig. 2B, Figs. S20B-S21B), in which from the second scan, an additional reduction peak appeared between the first reduction and second reduction of W^{VI} to W^{V}. Because **H_2T_2P** was easier to be reduced (first and second ring reduction at -1.20 V and -1.66 V *vs.* SCE for the porphyrin monomer) than **ZnOEP** (first ring reduction at -1.66 V *vs.* SCE), **poly-$PW_{11}Si_2$-H_2T_2P** presented also two waves corresponding to the first and second reduction of the **H_2T_2P** subunits (peaks d and e, Fig. 4A), whereas in the case of **poly-$PW_{11}Si_2$-ZnOEP** only the first reduction of the **ZnOEP** subunit was detectable at -1.81 V *vs.* SCE (Fig. S20A). Peaks d and e may correspond to the reduction of the macrocycle, however, the last reduction process (peak e) might also be the overlap of the signal of reduction of the porphyrin and the third reduction of the W^{VI} to W^{V} of the hybrid polyanion **Py-$PW_{11}Si_2$-Py** (see Table 1), which may explain why the current peak was higher.

In addition to the cathodic waves discussed above, **poly-$PW_{11}Si_2$-ZnOEP** and **poly-$PW_{11}Si_2$-H_2T_2P** also showed an anodic process at +1.24 V and +1.63 V measured from Figure S22A and Figure S22D respectively (Table 1) corresponding to the first oxidation of the porphyrin subunits.

Table 1. Electrochemical data for **ZnOEP**, **H_2T_2P**, **Py-$PW_{11}Si_2$-Py**, **Py-$P_2W_{17}Si_2$-Py**, **poly-$PW_{11}Si_2$-ZnOEP**, **poly-$PW_{11}Si_2$-H_2T_2P**, **poly-$P_2W_{17}Si_2$-ZnOEP** and **poly-$P_2W_{17}Si_2$-H_2T_2P**.

Compounds	Ring oxidation		Reduction of py^+ and of W^{VI}		Ring reduction	
ZnOEP [a]	1.08 (130)	0.71 (128)			-1.66	
H_2T_2P [a]	1.27	1.01			-1.20 (170)	-1.66 (320)
Py-$PW_{11}Si_2$-Py [a,GC]			-0.34 (75)	-0.87 (59)		
			-1.50 (84)			
Py-$PW_{11}Si_2$-Py [a,ITO]			-0.34 (91)	-0.88 (110)		
			-1.65 (445)			
Py-$P_2W_{17}Si_2$-Py [a, GC]			-0.57 (78)	-0.94 (78)		
			-1.45 (72)	-1.73 (105)		
Py-$P_2W_{17}Si_2$-Py [a, ITO]			-0.49 (286)	-0.90 (40)		
			-1.42 (25)	-1.76 (190)		
poly-$PW_{11}Si_2$-ZnOEP [b]	1.24 [irr]		-0.38 (130)	-0.81[irr]	-1.81[irr]	
			-0.91 (138)			
poly-$PW_{11}Si_2$-ZnOEP [c]	-		-0.53 (150)	≈ -0.88[irr]	-1.02[irr]	
poly-$PW_{11}Si_2$-H_2T_2P [b]	1.63 [irr]		-0.37 (60)	-0.75[irr]	-1.17 (133)	-1.70[irr]
			-0.89 (50)			
poly-$PW_{11}Si_2$-H_2T_2P [c]	-		-0.53[irr]	≈ -0.89[irr]	-1.06[irr]	
poly-$P_2W_{17}Si_2$-ZnOEP [b]	1.26 [irr]		-0.60 [irr]	-1.04 [irr]	-1.61[irr]	
poly-$P_2W_{17}Si_2$-ZnOEP [c]	-		-0.62 (60)	-0.78 (60)	-1.11 (60)	-1.21 (40)
poly-$P_2W_{17}Si_2$-H_2T_2P [b]	1.66 [irr]		-0.37[irr]	-0.68[irr]	-1.26[irr]	
poly-$P_2W_{17}Si_2$-H_2T_2P [c]	-		≈ -0.65[irr]	-0.79 V[irr]	-1.11[irr]	

[a] Potentials in V *vs.* SCE were obtained from cyclic voltammetry in 1,2-$C_2H_4Cl_2$ with 0.1 mol L^{-1} $TBAPF_6$. Scan rate = 100 mV s^{-1}. Working electrode: ITO, S=1 cm^2. See Figs. S9-S12. [b] Potentials in V *vs.* SCE were obtained from cyclic voltammetry in CH_3CN/1,2-$C_2H_4Cl_2$ (3/7) with 0.1 mol L^{-1} $TBAPF_6$. Scan rate = 100 mV s^{-1}.

[c] Potentials in V *vs.* SCE were obtained from cyclic voltammetry in H_2O with 0.5 mol L^{-1} NaI. Working electrode: glassy carbon electrode. Scan rate = 100 mV s^{-1} (see Fig. S23).

Working electrode: ITO, S=1 cm^2. The given half-wave potentials are equal to $E_{1/2} = (E_{pa} + E_{pc})/2$. Under bracket: $\triangle E_p = |E_{pa} - E_{pc}|$.

In the case of **Py-$P_2W_{17}Si_2$-Py**, the reductions of W^{VI} to W^V gave ill-defined waves, hardly observed on ITO electrode (Fig. 1). Similar ill-defined waves were also detected during the iterative scans (Fig. S16). In reduction, **poly-$PW_{17}Si_2$-H_2T_2P** gave three reduction peaks at -0.37 V, -0.68 V

and -1.26 V, respectively (peaks a, b and c in Fig. 4B). The two last reduction peaks can be the superposition of the reduction of the pyridinium and the **H_2T_2P** porphyrin with the POM, respectively.

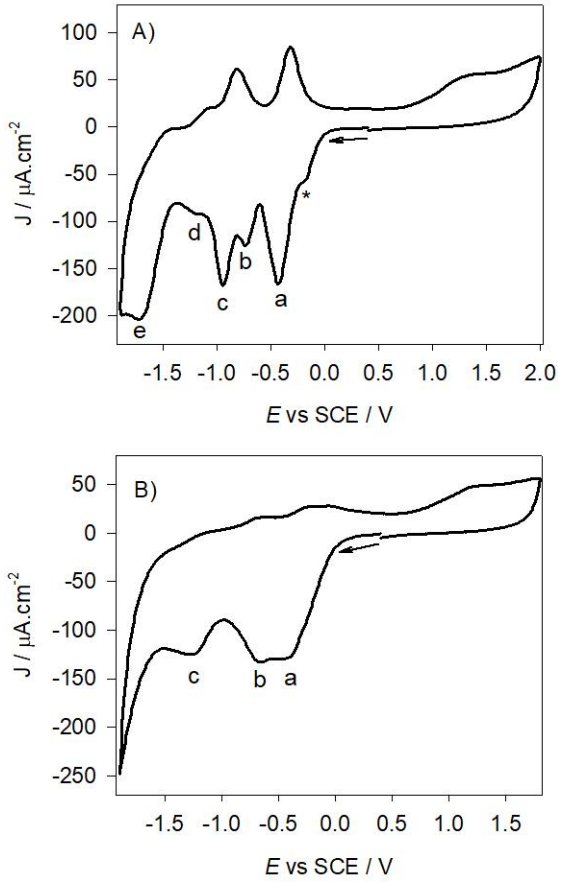

Figure 4. Cyclic voltammograms of A) **poly-$PW_{11}Si_2$-H_2T_2P** and B) **poly-$P_2W_{17}Si_2$-H_2T_2P** (obtained after 25 scans, between 0.00 V and +1.60 V) in CH_3CN/1,2-$C_2H_4Cl_2$ (3/7) with 0.1 mol/dm^3 NBu_4PF_6. (←) Start of the scan. S =1 cm^2; scan rate: 0.1 V/s. Peak *: reduction of the isoporphyrin.

On the reversal scan, first the oxidation and then the reduction, similar behaviour were observed (Fig. S22). Similarly, in addition to the catholic waves, **poly-$PW_{17}Si_2$-ZnOEP** and **poly-$PW_{17}Si_2$-H_2T_2P** also showed an anodic process at +1.26 V and +1.66 V respectively (Table 1) which corresponds to the first oxidation of the porphyrin subunits **ZnOEP** (Fig. S22C) and **H_2T_2P** (Fig. S22D).

3.5 UV-vis spectroscopy

The UV–visible absorption spectra of the porphyrin monomers (**H_2T_2P** and **ZnOEP**, black line) in solution and the **poly-$PW_{11}Si_2$-ZnOEP** (Figs. S24), **poly-$PW_{17}Si_2$-ZnOEP** (Fig. 5 and Fig. S26), **poly-$PW_{11}Si_2$- H_2T_2P** (Fig. S27) and the **poly-$P_2W_{17}Si_2$- H_2T_2P** (Fig. S28) copolymer films deposited on ITO are shown for comparison.

This superimposition reveals that the Soret band of **poly-$P_2W_{17}Si_2$-ZnOEP** copolymers, attributed to the main porphyrin-based π–π* electronic transition, is broader and red-shifted in copolymers (onto ITO electrode) (Table 2 and Fig. 5). Similar behaviour are observed for the other copolymers.

This evolution can be explained by the exciton coupling theory concerning intra- or intermolecular excitonic interactions between the porphyrin subunits, together with a greater deformation of the macrocycles within the polymer. After electropolymerization, the films were found to be fully soluble in DMF. Analysis of the resulting solutions by UV–vis absorption spectroscopy revealed a sharper Soret band and a slighlty lower hypochromatic shift than that recorded on the solid film (Figs. S34B-S36B and Fig. 5B). This evolution suggests that, for the most part, intramolecular interactions remain when the copolymers are in solution.

UV-visible absorption spectra of the mother solution, containing **ZnOEP** and **Py-POM-Py** (**Py-$PW_{11}Si_2$-Py** or **Py-$P_2W_{17}Si_2$-Py**), after the deposition of several films clearly show no demetallation of the starting **ZnOEP** and no demetallation of the **ZnOEP** units of the films (Fig. 5 and Figs. S24-S25).

The UV-vis absorption spectra of **poly-$P_2W_{17}Si_2$-ZnOEP** obtained with different iterative scans are displayed in Fig. 5A. Plotting the absorbance of the Soret band recorded for the four prepared films as a function of the number of iterative scans (insert Fig. 5A and Fig. S26) showed similar curves

featuring an increase reaching a plateau after nearly 25 scans. The films using **ZnOEP** as porphyrin subunit gave a higher absorbance intensity than hybrids using **H_2T_2P** after 25 iterative scans between 0 and +1.60 V *vs.* SCE.

Table 2. UV–visible spectral data for **ZnOEP** and **H_2T_2P** in DMF, **Py-$PW_{11}Si_2$-Py** and **Py-P_2W_{17} Si_2-Py** in CH_3CN. **poly-$PW_{11}Si_2$-ZnOEP**, **poly-$PW_{11}Si_2$-H_2T_2P**, **poly-$P_2W_{17}Si_2$-ZnOEP** and **poly-$P_2W_{17}Si_2$-H_2T_2P** on ITO and in DMF. In brackets: molar extinction coefficient (ε /10^3 $dm^3 \cdot mol^{-1} \cdot cm^{-1}$).

Compound	Soret band /nm	Q bands / nm	O to W charge transfer bands (LMCT) / nm
ZnOEP	408 (672.3)	538 (34.3), 674 (37.7)	
H_2T_2P	407 (402.3)	502 (16.6), 537 (5.8), 577 (4.6), 631 (1.4)	
PW_{11}			268 (57.9), 335 (63.0)
P_2W_{17}			288 (142.4), 305 (135.2)
poly-$PW_{11}Si_2$-ZnOEP(ITO)	426	552, 586	
poly-$PW_{11}Si_2$-ZnOEP(DMF)	424	551, 582	271, 286, 306
poly-$PW_{11}Si_2$-H_2T_2P (ITO)	425	521, 559, 591, 658	
poly-$PW_{11}Si_2$-H_2T_2P (DMF)	426	509, 549, 586, 643	271, 285, 305
poly-$P_2W_{17}Si_2$-ZnOEP(ITO)	426	555, 589	
poly-$P_2W_{17}Si_2$-ZnOEP(DMF)	422	554, 586	290, 308
poly-$P_2W_{17}Si_2$-H_2T_2P (ITO)	425	517, 557, 594, 654	
Poly-$P_2W_{17}Si_2$-H_2T_2P (DMF)	422	515, 555, 590, 652	291, 307

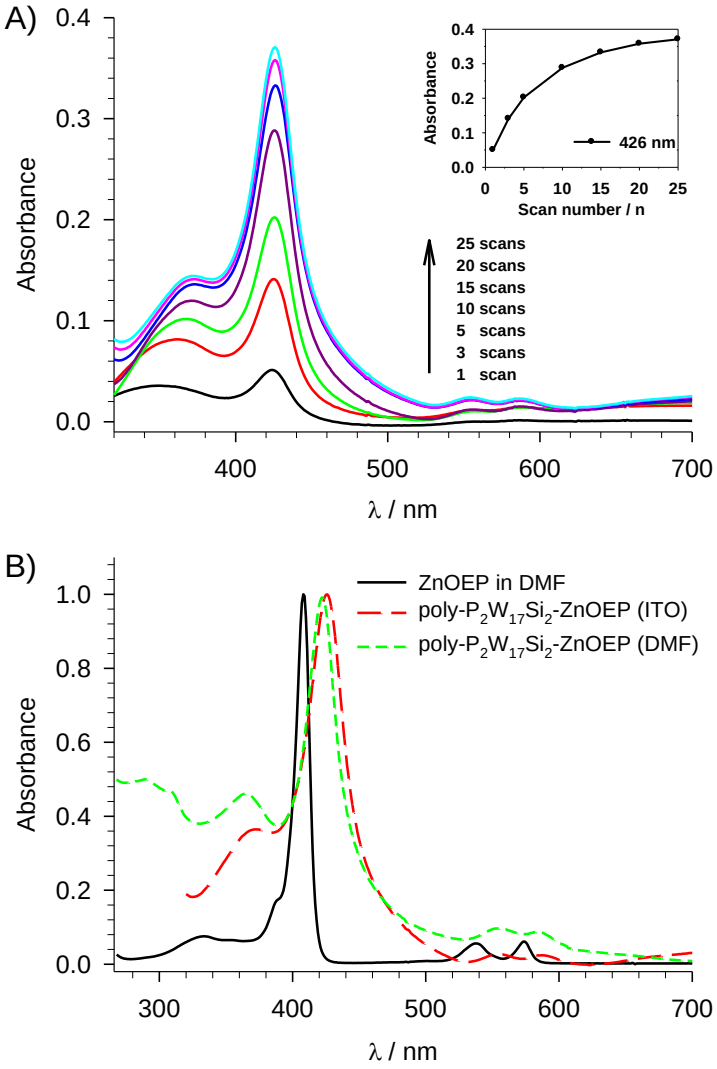

Figure 5. A) UV–vis spectra of **poly-$P_2W_{17}Si_2$-ZnOEP** obtained after n iterative scans (n = 1, 3, 5, 10, 15, 20 and 25) on ITO. Insert: Plot of the intensity of the absorbance of the Soret band *versus* the iterative scan number between 0 and +1.60 V *versus* SCE. B) Normalized UV-vis spectra of **ZnOEP** (black line) in DMF, **poly-$P_2W_{17}Si_2$-ZnOEP** on ITO (red line)**, poly-$P_2W_{17}Si_2$-ZnOEP** in DMF (green line).

3.6 X-ray photoelectron spectroscopy (XPS)

Although XPS measurements give only a semi quantitative elemental analysis, the C, N, O, P, W, Si, Zn and F elements enabled to confirm the presence of these elements in the copolymer.

XPS spectra of **poly-$P_2W_{17}Si_2$-ZnOEP** copolymers are presented in Figure 6 (see Figures S38-S40 for the other copolymers). For example, the Zn 2p3/2 (1023.2 eV) was assigned to the zinc atom in

ZnOEP (Fig. 6).

Two peaks for the nitrogen (N 1s) were observed, which appeared at 399.0 eV, and 402.4 eV corresponding to three types of nitrogen atoms: the nitrogen of the porphyrin, the pyridinium spacer, and the TBA counter cation. However, owing to the higher charge of Dawson-type POMs subunit (-6) compared to that of Keggin-type POMs subunit (-3), the N1s of **poly-$P_2W_{17}Si_2$-ZnOEP** (Fig. 6) and **poly-$P_2W_{17}Si_2$-H_2T_2P** (Fig. S29) hybrids were dominated by the ammonium peak at 402.4 eV and even overlapped other peaks. In the case of **poly-$PW_{11}Si_2$-ZnOEP** and **poly-$PW_{11}Si_2$-H_2T_2P** (Figs. S38-S39) with Keggin-type POMs displaying lower charge, three types of nitrogen (N 1s) with different chemical states were indeed detected at 398.6 eV, 400.0 eV and 402.3 eV and 398.4 eV, 400.2 eV and 402.2 eV respectively. The two first signals were attributed to the nitrogen of the porphyrin and the pyridinium spacer, while the peaks at higher binding energy are related to the ammonium group of the TBA counter-ion.

Poly-$P_2W_{17}Si_2$-ZnOEP exhibited other peaks corresponding to W 4f (36.1 eV for W 4f7/2 and 38.2 eV for W 4f5/2) peaks, O 1s (532.6 eV) coming from the POM part of the copolymer (**$P_2W_{17}Si_2$**) while the O 1s signal (530.9 eV) came from H_2O on the copolymer surface. The F 1s (687.0 eV) was ascribed to counter anion PF_6^-, suggesting that the charged pyridinium did not act as counter-ion of the POM subunits. The P 2p3/2 (133.8 eV) was either ascribed to the counter-ion PF_6^- and the POM heteroatom. Finally, when we replaced **ZnOEP** by **H_2T_2P**, the Zn 2p3/2 signal disappeared (Figs. S29-S31) as expected.

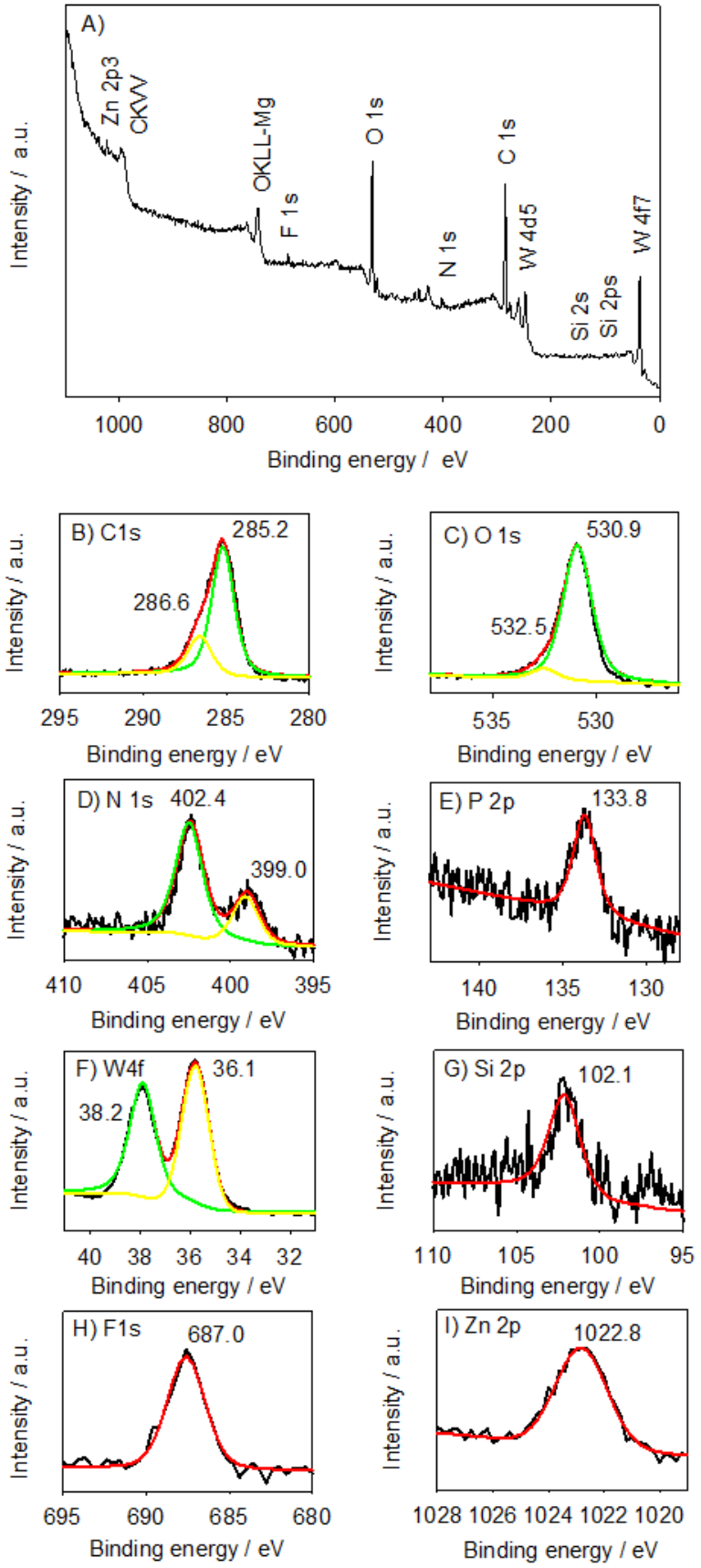

Figure 6. XPS of **poly-$P_2W_{17}Si_2$-ZnOEP** survey XPS spectra (A), C 1s (B), O 1s (C), N 1s (D), P 2p (E), W 4f (H), Si 2p (G), F 1s (H), Zn 2p (I).

3.7 Film Morphology (Atomic Force Microscopy)

The coated electrodes were washed with CH_2Cl_2 to remove any residual of the conducting salt ($TBAPF_6$) present on the film. In a typical image, **poly-$P_2W_{17}Si_2$-ZnOEP** and **poly-$P_2W_{17}Si_2$-H_2T_2P** appeared as tightly packed coils with average diameters of 60 ± 5 nm and 75 ± 5 nm and a height of 11.2 ± 0.3 nm and 7.9 ± 0.3 nm (Fig. 7), respectively. The root mean square (RMS) surface roughness of the film obtained after 25 iterative scans from 0 to +1.60 V *vs.* SCE were 1.9 and 2.3 nm in an area of 1 μm^2 for **poly-$P_2W_{17}Si_2$-ZnOEP** and **poly-$P_2W_{17}Si_2$-H_2T_2P**, respectively.

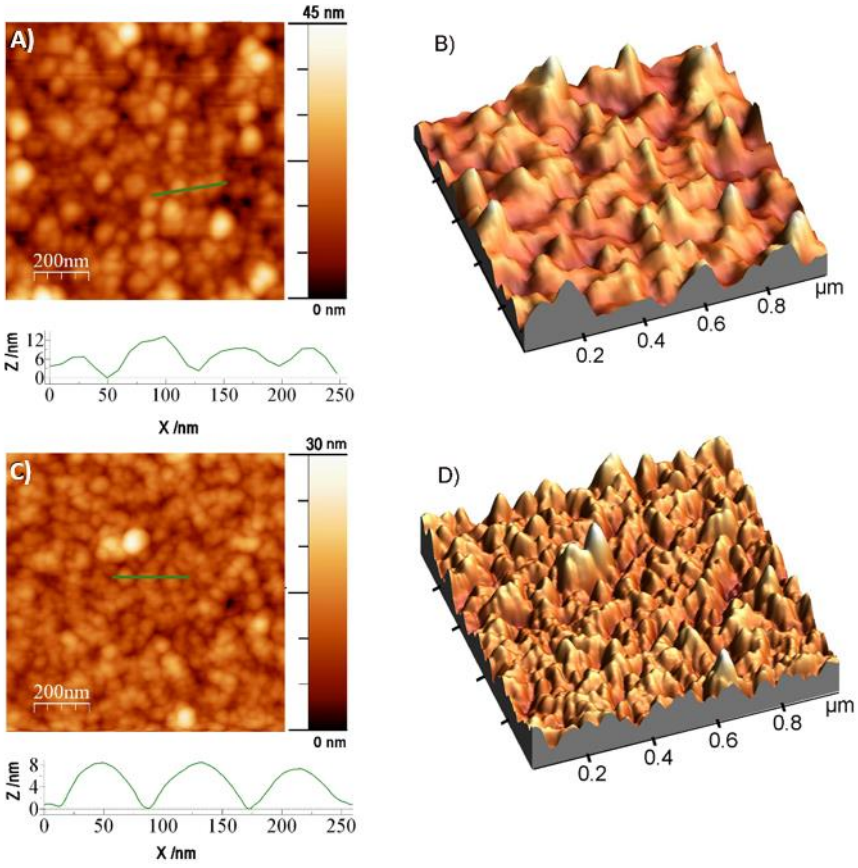

Figure 7. Tapping mode AFM topography of A) and B) **poly-$P_2W_{17}Si_2$-ZnOEP**, and C) and D) **poly-P_2W_{17}-H_2T_2P** films and section analysis of the aggregate marked.

When using **Py-$PW_{11}Si_2$-Py** as Py-POM-Py unit instead of **Py-$P_2W_{17}Si_2$-Py**, the size of the tightly packed coils was smaller. The average diameters were 45 ± 5 nm and 55 ± 5 nm, and the height were

2.9 ± 0.2 nm and 3.8 ± 0.2 nm for **poly-$PW_{11}Si_2$-ZnOEP** and **poly-$PW_{11}Si_2$-H_2T_2P** (Fig. S32), respectively. RMS surface roughness of the film obtained after 25 iterative scans were 1.9 and 2.3 nm in an area of 1 μm^2 for **poly-$P_2W_{11}Si_2$-ZnOEP** and **poly-$PW_{11}Si_2$-H_2T_2P**, respectively.

Note that the coils were not observed in the case of the bare ITO electrode and are thus attributed to the copolymers (Fig. S33).

To measure the thickness of the coated film on ITO, we removed the copolymer by scratching the film with a metallic tip. We observed some puffiness induced by the removal of the material. Analysis of the bottom proved that the ITO substrate was damaged. The thickness was the height difference on each side, far from the puffiness. The estimated thickness increased with increasing number of scans, following the nearly same trend as the UV/Vis absorbance intensity (Fig. 8).

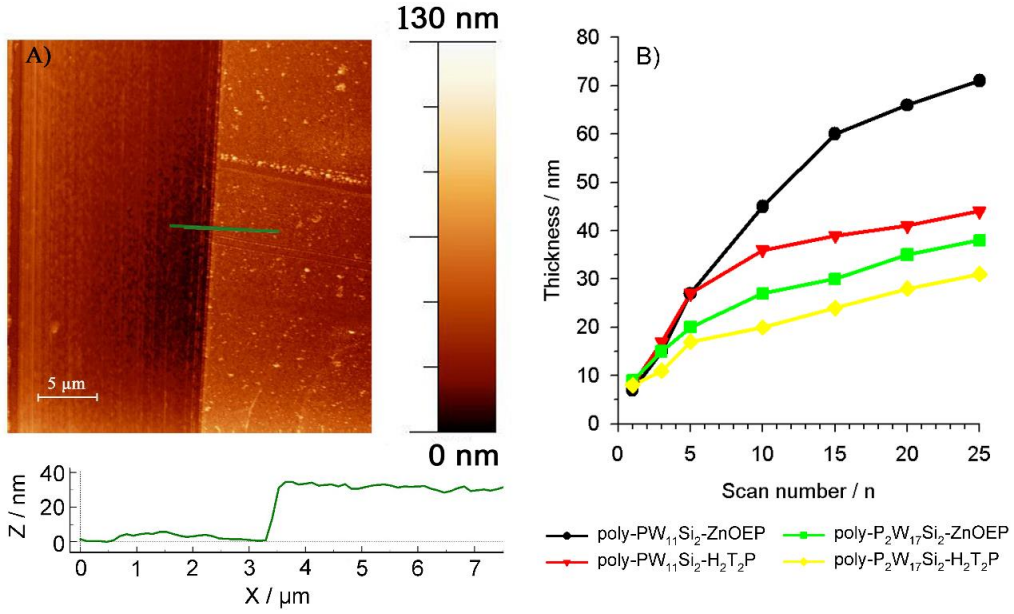

Figure 8. A) AFM image of the ITO electrode modified with **poly-$P_2W_{17}Si_2$-ZnOEP** obtained after 25 iterative scans from 0 to +1.60 V *vs.* SCE. Bottom: section analysis. B) Thickness measured by AFM versus different numbers of iterative scans for the four copolymers

3.8 Photoelectrochemical response under visible illumination

The influence of the film thickness, once deposited on ITO electrodes, on the photocurrent generation

under visible light illumination was further investigated. Figure 9 shows amperometric J–t curves for the photocurrent response for a set of **poly-$P_2W_{17}Si_2$-ZnOEP** films with various potential scan numbers performed during the electropolymerization step. The hybrids films supported on ITO electrodes were immerged in aqueous solutions and left under visible light (λ > 385 nm; the POM subunits not absorbing in this domain). The photocurrent was measured in the presence of NaI_3 (5 mmol.L^{-1})/NaI (0.5 mol.L^{-1}) as reversible redox mediator. The bias potential was set at 0.00 V *vs.* the Pt counter electrode, which can be considered to be in a first approximation at the I_3^-/I^- equilibrium potential. The cell was successively exposed to visible light for 1 minute followed by the dark for 1 minute. The obtained photocurrent is negative whatever the number of potential scans, indicating that the hybrid POM-porphyrin film is acting as a photocathode by reducing I_3^- into I^-. Interestingly, the magnitude of the photocurrent depended on the number of deposition cycles performed for the preparation of the films. The magnitude of the photocurrent increased appreciably from n=1 to n=3, but for number of deposition cycles above 3, the photocurrent magnitude decreased.

Electrochemical impedance spectroscopy (EIS) is a powerful technique for the investigation of the electronic and ionic processes in dye-sensitized solar cells **[27]**.-From the analysis of the Nyquist plot, the charge transfer resistance R_{ct} of the electron transfer as well as the parameters of the charge transport in the porous electrode and of the recombination reaction caused by the back electron transfer from the I^- species to the electrode can then be extracted. Note that the hundred times higher I^- concentration in the electrolyte (0.5 mol L^{-1}) compared to I_3^- (5 mmol L^{-1}) is expected to increase the kinetics of the recombination. The Nyquist diagrams displayed in Fig. 10 features only one semi-circle, resulting from the coupling of the capacitance of the electrode with the charge transfer resistance either from the ITO to the I^-/I_3^- species in the electrolyte at the electrode/electrolyte interface.

As shown in Figure 9, the photocurrent magnitude and the values of R_{ct} measured either in the dark or under illumination followed the same trend under the same measurement conditions. It suggested that the trend observed in the photocurrent generation efficiency is driven by the variation of the charge transfer resistance from the film to the electrolyte to some extent, whereby the best performance for **poly-$P_2W_{17}Si_2$-ZnOEP** film was obtained by only three iterative scans between 0.00 and +1.60 V v*s.* SCE. The improvement in the efficiency of the photovoltaic process with the increasing number of iterative scan ($1 < n \leq 3$) is probably due to the increase of the amount of electroactive and photoactive materials in good electrical contact with the ITO substrate as revealed by the decrease of the R_{ct} value. In contrast, the decrease of the photocurrent and the increase of the charge transfer resistance R_{ct} for $n > 3$ might be attributed to less efficient electron transfer to I_3^- and less efficient mass transport of I_3^- in the film when the thickness of the polymer hybrid film increases.

Figure 10B shows I/V curve of **poly-$P_2W_{17}Si_2$-ZnOEP** (prepared with n = 3 scans between 0.00 V and +1.60 V *vs.* SCE) in the same measuring environment. Under irradiation the current magnitude increased a little and the difference between light on and light off correspond to the photocurrent. Under illumination, the charge transfer resistance decreases which might be attributed to the small increase of the OCP (ca. 10 mV) and/or to the local increase of the temperature caused by the light absorption by the photoactive film.

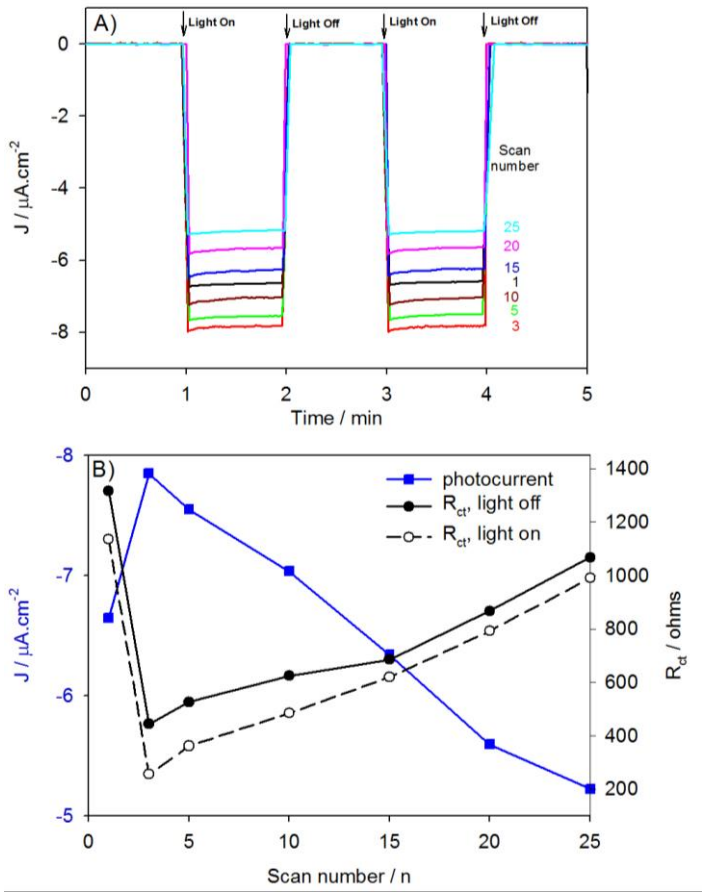

Fig. 9 A) Photoelectrochemical response of **poly-$P_2W_{17}Si_2$-ZnOEP** with different numbers of iterative scans used for the preparation of the film (between 0.00 V and +1.60 V *vs.* SCE). Only one side is recovered by ITO with on-off light illumination from 300 W Xe Arc lamp (with $\lambda \geq 385$ nm long pass filter; back illumination). BIAS potential: 0.00 V *vs.* Pt counter electrode. B) (■) plots of the photocurrent, and plots of R_{ct} without illumination (●), and with illumination (○) in aqueous solution containing I_3^- 5 mmol L^{-1} and I^- 0.5 mol L^{-1} *versus* the numbers of iterative scans.

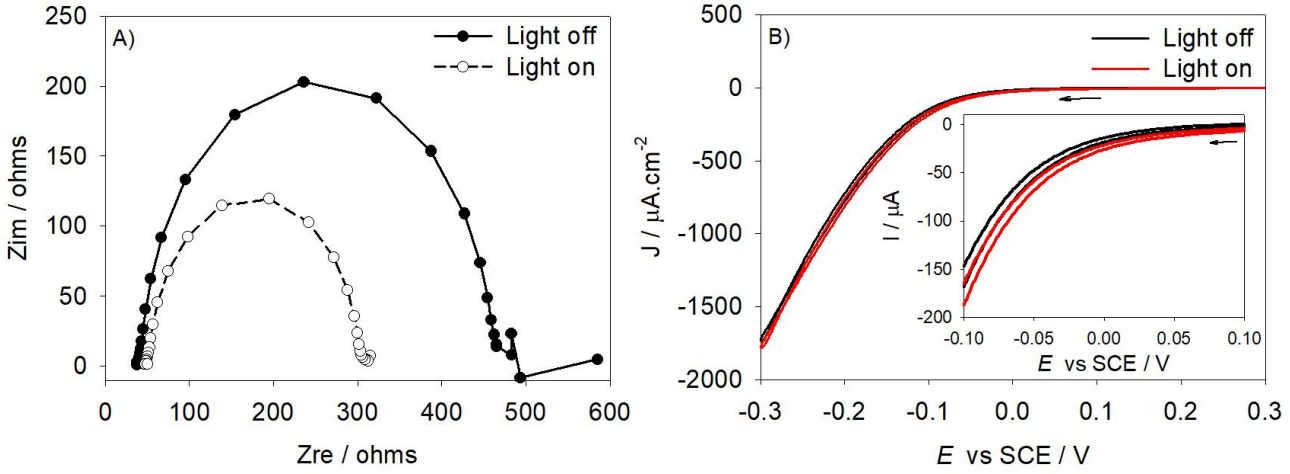

Fig. 10 A) Nyquist plot and B) I/V curve of **poly-$P_2W_{17}Si_2$-ZnOEP** (prepared with n = 3 scans between 0.00 V and +1.60 V *vs.* SCE) without and with illumination from 300 W Xe Arc lamp (with $\lambda \geq 385$ nm long pass filter; back illumination) in H_2O containing I_3^- 5 mmol L^{-1} and I^- 0.5 mol L^{-1}. The impedance measurements were performed at OCP in the dark and under illumination.

The electrodes were tested under on-off light illumination during 60 minutes at short circuit showing good stability of the performance and of film under operation. (Figs. S38-41).

We have measured photocurrent generation using various positions of the ITO substrate: in front or back illumination and back illumination with reverse position (Scheme S1 and Figs. S38-S42). The best position is for the back illumination. In the case of the in front illumination with reverse position, one part of the photon is absorbed by the I_3^- present in the solution and don't reach the ITO substrate showing important decrease of the photocurrent. In the case of the in front illumination, slight decrease of the photocurrent is also noticed.

3.9 Effect of the type of polyoxometalates and of porphyrins

The studies of the silyl-and tin derivatized Keggin- and Wells-Dawson-type POMs revealed limited electronic communication between the organic and inorganic parts in the ground state, while the electron acceptor character of the POMs depended on its structural class and the nature of the chemical anchor (Si *versus* Sn) **[12,28-29]**. When comparing the photophysical properties of a series of POM-Ir hybrids, some of us concluded that the Ir-cyclometalated silyl-Dawson hybrid was the most promising candidate in photoelectron transfer since it provided a good compromise between the efficient charge separation rate and long lived charge recombination [**28a]**.

In the present work, the electrochemical impedance spectra of the four prepared films have been measured in H_2O containing I_3^- 5 mmol L^{-1} and I^- 0.5 mol L^{-1} under visible irradiation. In all cases, the magnitude of the photocurrent increased appreciably from n=1 to n=3-5, then for number of deposition cycles above 5, the photocurrent magnitude decreased. In order to compare the efficiency of the four copolymers, films with similar thickness (Fig. 8B) were studied and compared. All the films were fabricated using iterative scans between 0.00 V and +1.60 V *vs.* SCE. **poly-PW_{11}-ZnOEP** and **Poly-PW_{11}-H_2T_2P** films were obtained using 3 scans (thickness: 15 nm and 17 nm, respectively), while

poly-P_2W_{17}-ZnOEP and **poly-P_2W_{17}-H_2T_2P** copolymers were fabricated using 5 scans (thickness: 20 nm and 17 nm, respectively). This confirms that the pyridiniums subunit plays a role in the kinetics of the charge separation process, and then in the mechanism of the photocurrent generation (Fig. 12).

Similar photoelectrochemical behaviors were obtained for **poly-$P_2W_{17}Si_2$-H_2T_2P** (Fig. S37), **poly-$PW_{11}Si_2$-ZnOEP** (Fig. S35 and Fig. S36A) and **poly-$PW_{11}Si_2$-H_2T_2P** (Fig. S36B). The best photocurrent was obtained for **poly-$P_2W_{17}Si_2$-ZnOEP** (obtained after 3 iterative scans) which exhibited also the lowest R_{ct} (Fig. 11) of the four copolymers. The differences in the R_{ct} values between the four copolymers might be tentatively ascribed to possible structural differences. It is also worth mentioning that the copolymer **poly-$P_2W_{17}Si_2$-ZnOEP** with the lower R_{ct} exhibits also a more reversible redox potential wave of pyridinium subunits compared to the other copolymer (see Fig. S23). With regards to the open circuit photovoltage, it of ca. 40 mV *vs.* the I_3^-/I^- redox equilibrium potential for the **poly-$PW_{11}Si_2$-H_2T_2P** copolymer, and of approximately 10 mV for **poly-$P_2W_{17}Si_2$-H_2T_2P**, **poly-$P_2W_{17}Si_2$-ZnOEP** and **poly-$PW_{11}Si_2$-H_2T_2P** copolymers. Note that the poly-$P_2W_{17}Si_2$-ZnOEP copolymer exhibits a low photovoltage despite of much higher photocurrent. This might be due to the fast recombination kinetics with I- species.

Additionally, in this series of photoactive assemblies, highest photocurrent magnitudes were always measured in the case of copolymers with **ZnOEP** porphyrin but only for the comparison with the same type of POM (Fig. 11B). It may be explained in part by the molar extinction coefficient of **ZnOEP**, which is higher than for **H_2T_2P**. In such a case, the visible light collection ability of the POM-**ZnOEP** copolymers is better than for POM-**H_2T_2P** for the same type of POM. Furthermore, when changing the type of POM: **$P_2W_{17}Si_2$** *versus* **$PW_{11}Si_2$** the measured photocurrent magnitude was highest in the case of the Dawson type POM (**$P_2W_{17}Si_2$**). This result suggests that the nature of the POM in the

copolymer also affects the efficiency of the photocurrent generation by changing the redox behavior and the kinetics of the charge transfer processes of the film.

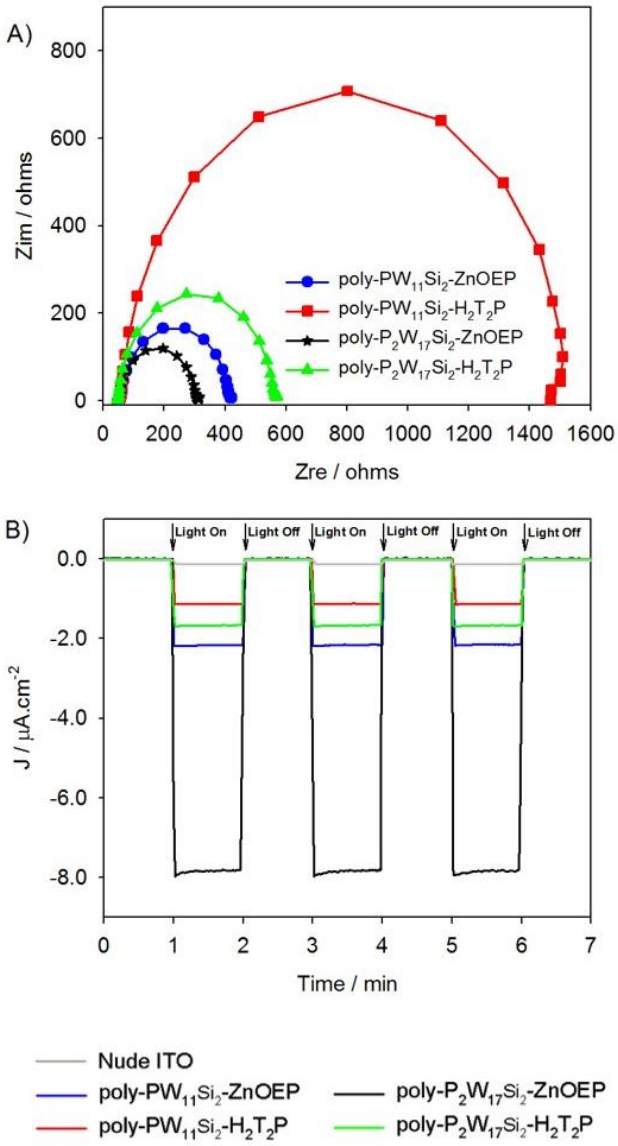

Figure 11. A) Nyquist plot and B) photoelectrochemical response of **poly-$PW_{11}Si_2$-ZnOEP** (5 scans, thickness: 15 nm), **poly-$PW_{11}Si_2$-H_2T_2P** (5 scans, thickness: 17 nm), **poly-$P_2W_{17}Si_2$-ZnOEP** (3 scans, thickness: 20 nm) and **poly-$P_2W_{17}Si_2$-H_2T_2P** (3 scans, thickness: 17 nm) (preparation of the film between 0.00 V and +1.60 V *vs.* SCE) under irradiation from 300 W Xe Arc lamp (with $\lambda \geq 385$ nm long pass filter; back illumination) in H_2O containing I_3^- 5 mmol L^{-1} and I^- 0.5 mol L^{-1}. The impedance spectra were measured in the dark at the OCP.

Table 3. Comparison of the magnitude of the photoelectrical responses (see Fig. S36 in Supporting Information for the representation of the various ruthenium complexes, hemicyanines, phtalocyanines, PVP or porphyrins).

	Systems	Ref	J ($\mu A.cm^{-2}$)	BIAS	Conditions
Ru / POM	**$[Ru(bpy)_3]^{2+}$/ $[W_{18}O_{54}(SO_4)_2]$**	**30**	59.0	+1.00 V[a,c]	BnOH in CH_3CN 350 W Oriel Arc lamp, λ>400 nm
	Ru-Co-P / S_2Mo_{18} **Ru-PVP / S_2Mo_{18}**	**31**	0.01 0.04	+0.40 V[a,c] +0.40 V[a,c]	BnOH in CH_3CN 350 W Oriel Arc lamp,λ>488 nm
	$[Ru(bpy)_2$-$(PVP)_{10}]$ / $[S_2Mo_{18}]$ **$[Ru(bpy)_2$-$(PVP)_{10}]$ / $[P_2W_{18}]$** [3]	**32**	0.04 0.24	+0.80 V[a,c] +0.80 V[a,c]	BnOH in CH_3CN 350 W Xe Arc lamp, λ>480±5 nm
	Polymer / $(W_{72}V_{30}/PPV)_{10}$[d]	**33**	1.7	0.00 V[c]	O_2 in H_2O 100 W Xe Arc lamp (UV and visible)
Hemicyanine / POM	**Hemicyanine / SiW12/H3**	**34**	-1.0	-0.20 V	EV^{2+} [e] or O_2 in H_2O 500 W Xe Arc lamp, 325 <λ< 730 nm
	Hemicyanine / $Cd_4(PW_9)_2/N^6$	**35**	-2.4	-0.30 V	MV^{2+} [e] or O_2 in H_2O 500 W Xe Arc lamp, 325 <λ< 730 nm
	Hemicyanine / $Ni_4(PW_9)_2/H^6$	**35**	-3.5		
	Hemicyanine / $Cu_4(PW_9)_2/H^6$	**36**	-3.7		
	Hemicyanine / $Zn_4(PW_9)_2/H^6$	**36**	-2.5		
	Hemicyanine / $Zn_4(PW_9)_2/N^3$	**37**	-13.7		
Phtalocyanine / POM	**Phtalocyanine / P_2Mo_{18}/CoTAPc**[f]	**38**	0.03	+0.56 V[c]	O_2 in H_2O, 5 W λ = 365 nm
	Phtalocyanine / $SiMo_{12}$/CuPc[f]	**39**	0.6	+0.56 V	O_2 in H_2O, 300 W Xe arc lamp
Porphyrin / POM	**Porphyrin / $P_2V_3W_{15}$-TPP**[g]	**40**	-1.0	+0.10 V[c]	I_3^-/I^- in H_2O 300 W Xe Arc lamp, λ> 385 nm
	Porphyrin / FeP_2W_{17}/ $H_2TPhN(Me)_3P)_{25}$	**41**	-1.8	-0.10 V[c]	I_3^-/I^- in CH_3CN 300 W Xe Arc lamp, λ> 385 nm
	poly-$[P_2W_{15}V_3]$-m3,3-ZnOEP	**9**	-2.8	-0.10 V	I_3^-/I^- in H_2O 300 W Xe Arc lamp, λ> 385 nm
	poly-$[P_2W_{15}V_3]$-l3,3-ZnOEP	**9**	-0.9		
	poly-$[P_2W_{15}V_3]$-l4,4-ZnOEP	**9**	-3.1		
	poly-$PW_{11}Si_2$-ZnOEP[h]	this work	-2.2	0.00 V	I_3^-/I^- in H_2O 300 W Xe Arc lamp, λ> 385 nm
	poly-$PW_{11}Si_2$-H_2T_2P[h]	this work	-1.1		
	poly-$P_2W_{17}Si_2$-ZnOEP[h]	this work	-7.8		
	poly-$P_2W_{17}Si_2$-H_2T_2P[h]	this work	-1.7		

[a] The [Ru–POM] adduct is excited by incident light to become [Ru–POM]*. This excited [Ru–POM]* species forms is a pre-associated (POM—BnOH) before photo-oxidation of benzylalcohol (BnOH) occurs by hole transfer. Then reoxidation of the reduced [Ru–POM] catalyst occurs at the electrode interface which require high applied potential. [b] Layer-By-Layer (LBL). [c] Three electrodes set up using applied potential versus SCE. [d] Poly(p-phenylenevinylene) derivatives (PPV).[e] Ethylviologen (EV^{2+}), Methylviologen (MV^{2+}). [f] Phtalocyanine (Pc). [g] Tetraphenylporphyrin (TPP). [h] This work.

The measured intensity of the generated photocurrent was in the same order of magnitude or somewhat higher than those in previous reports on porphyrin/POM excepted in the case of **poly-$P_2W_{17}Si_2$-ZnOEP** where the efficiency is more than doubled compared to the values reported in the literature (Table 3) **[41,40,9]**. Comparable photoelectrochemical responses have also been reported in the

literature for various chromophore/POM assemblies, such as poly(p-phenylenevinylene)/POM **[33]** or photosensitizer/POM (photosensitizer: ruthenium complexes **[30-32]**, hemicyanine **[37-35]**, phthalocyanine; see Table 3 and Supporting Information, Figure S42) **[30-32,38-39,42]**. However, a more comprehensive comparison is difficult because of the extensive variation of the measurement conditions like for instance, the BIAS value, the solvent or the power of the lamp used.

3.10 Energy diagram of the electron transfer processes

To discuss in more details, the photocurrent generation mechanism in the system, we estimated the energies of the relevant electronic states. In the case of copolymer **poly-$P_2W_{17}Si_2$-ZnOEP**, an energy level diagram can be built using the oxidation potential of **ZnOEP** subunit and the reduction potential of W^{VI}/W^{V} of the POM cluster and the reduction potential of pyridinium subunits, together with the optical excitation of **ZnOEP** within the film (left part of Fig. 12, full line). It describes the thermodynamics of the system for spectral sensitization of the ITO electrode. From the electron affinity, the conduction band (E_c) edges of the ITO electrode surface was estimated to be ca. -4.5 eV in the literature **[43]**. In our conditions of the measurements, with BIAS potential of 0.00 V, the ITO and the Pt counter-electrode are maintained at the same potential. The calculated level of the ITO conduction band (E_c) edges of the ITO electrode surface is -4.50 – $E(I_3^-/I^-)$, which gives -5.13 eV ($E(I_3^-/I^-)$ = +0.63 V *vs.* NHE). The level of the excited porphyrin (–3.77 eV for $P^{+\bullet}/P^{*}$) and the ground state porphyrin (–6.00 eV for $P^{+\bullet}/P$) for the film were taken in reference to the oxidation potential of the porphyrin (+1.50 V *vs*. ENH with a band gap of 2.23 eV at λ = 555 nm; measured from the film). The energy level of the couples W^{VI}/W^{V}, $Py^{+}/Py^{\bullet}$ and I_3^-/I^- on the absolute scale were –4.12 eV (corresponding to

–0.38 V *vs.* NHE), –3.96 eV (corresponding to –0.54 V *vs.* NHE), and –5.13 eV (corresponding to +0.63 V *vs.* NHE) as represented in Fig. 12. Since it is really difficult to measure the redox potentials of **poly-$P_2W_{17}Si_2$-ZnOEP** using ITO electrode in aqueous solution, we have electropolymerized the **poly-$P_2W_{17}Si_2$-ZnOEP** film on the glassy carbon substrate, and then measured the cyclic voltammogram of the obtained film in the aqueous solution containing NaI as the conducting salt (Fig. S22). Nevertheless, the oxidation potentials of the porphyrin were not measurable in aqueous solution because of the water oxidation limitation. Thus, in the schematic energy level diagram, we have used the potentials determined in organic solvent.

The **$P_2W_{17}Si_2$** subunit acted as a good electron acceptor and could oxidize the pyridyl radical initially formed by electron transfer from the excited porphyrin to the pyridinium. The reduced POM could then in turn reduce I_3^-, while I^- could be reoxidized at the platinum counter electrode (Fig. 12, full line). The **$P_2W_{17}Si_2$** subunit therefore participated to the electron relay via a downhill electrochemical cascade and enhanced the charge separation distance (oxidized porphyrin and reduced POM), which hampered the charge recombination.

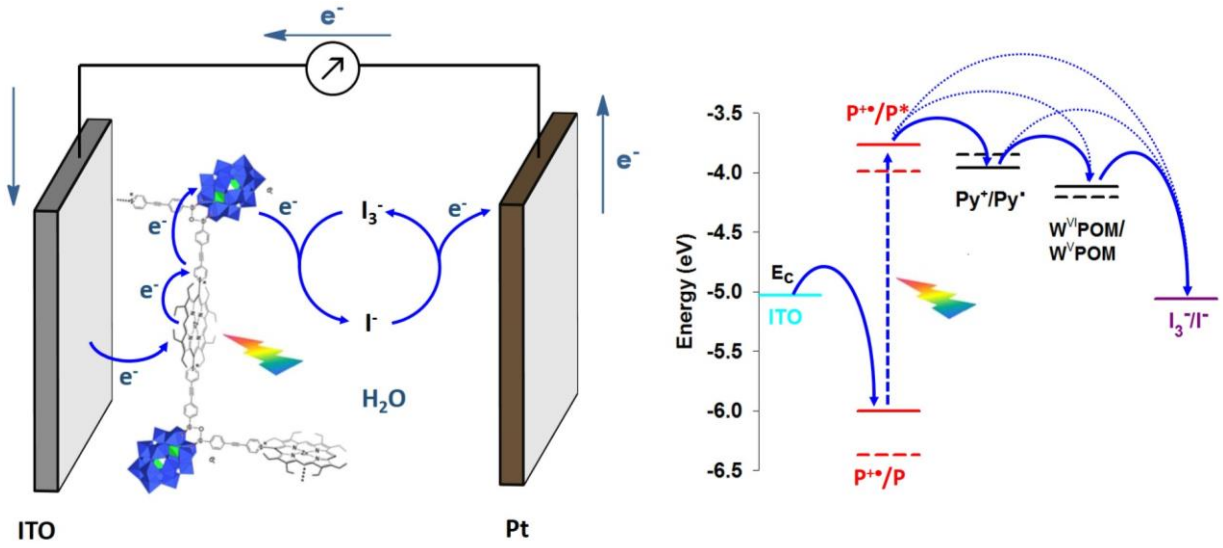

Figure 12. Schematic energy level diagram showing the electron transfer process calculated for **poly-$P_2W_{17}Si_2$-ZnOEP** (full line) and **poly-$P_2W_{11}Si_2$-H_2T_2P** (dotted line). P = porphyrin.

In the case of copolymer **poly-$PW_{11}Si_2$-H_2T_2P**, the energy level of the excited free base porphyrin **H_2T_2P** (–3.98 eV for $P^{+\bullet}/P^*$) and the ground state porphyrin (–6.37 eV for $P^{+\bullet}/P$) for the film were much lower than for **ZnOEP** (Fig. 12, dotted line). The energy level of the couples W^{VI}/W^V, $Py^+/Py^\bullet$ on the absolute scale were –4.21 eV (–0.29 V *vs.* NHE), and –3.85 eV (–0.65 V *vs.* NHE), as represented in Fig. 12 (dotted line), the energy level of I_3^-/I^- being unchanged. In this case, the electron transfer can occur either directly from the excited porphyrin to I_3^- or be relayed by the pyridinium and the POM. For **poly-$PW_{11}Si_2$-H_2T_2P**, the excited **H_2T_2P** free base porphyrin was not able to reduce the pyridinium and to exchange electron directly to the **$PW_{17}Si_2$** subunit, giving the reduced POM, which in turn could reduce the I_3^- in I^- that was further reoxidized at the platinum counter electrode (Fig. 12, full line). As the level of the excited porphyrin is higher for **ZnOEP** than for **H_2T_2P**, the driving force allowing the charge injection to the POM is higher with this porphyrin. This can explain the higher efficiency of the photocurrent generation using the zinc porphyrin. Furthermore, in case of the free base porphyrin, the pyridinium spacer should not participate to the electron relay, which may also explain its lower efficiency of the photocurrent generation.

For both porphyrins, the silyl-derivatized Dawson hybrids are more efficient than their Keggin analogues. Similarly, in the previously reported series of POM-Ir **[12,28]**. we observed that the Dawson-based hybrids displayed charge-separated state with slower charge recombination, compared to the Keggin analogues, due to their higher energy. The higher efficiency of the Dawson-porphyrin *vs.* the Keggin-porphyrin copolymers could then arise from a higher HOMO-LUMO gap, giving rise to charge separated states of longer lifetime.

4. Conclusion

Electropolymerization of organosilyl Keggin and Dawson-type POM derivatives bearing two pyridyl moieties with **ZnOEP** and **H_2T_2P** allowed us to prepare four covalently bonded POM-porphyrin copolymers. In this series of photoactive assemblies, the redox behavior of the POM, acting as an electron acceptor, could be tuned according to its structural class (Keggin *vs.* Dawson). The properties of the porphyrin (molar extinction coefficient: **ZnOEP** > **H_2T_2P**) dominated the light collection ability of the POM-porphyrin copolymers, and the order of the visible absorbance magnitude: **poly-$PW_{11}Si_2$-ZnOEP** > **poly-$PW_{11}Si_2$-H_2T_2P**, **poly-$P_2W_{17}Si_2$-ZnOEP** > **poly-$P_2W_{17}Si_2$-H_2T_2P**.

The impedance measurements indicated that **poly-$P_2W_{17}Si_2$-ZnOEP** copolymer had the lowest charge transfer resistance and the best performance for the photocurrent generation upon visible light illumination. This was attributed to the higher reducing power of the excited state of **ZnOEP** compared to **H_2T_2P** and the higher HOMO-LUMO gap with the Dawson system likely giving rise to charge separated states of longer lifetime. Monitoring the thickness of the film was found to be critical for the photocurrent-generation efficiency, probably due to the modification in conductivity of the deposited polymer.

Further developments must address the *in situ* measurement of the conductivity. The overall conversion efficiency η of the sealed cell needs in the future to be determined. Improving the conductivity of the films will be also important. One possibility is the introduction of gold nanoparticles onto the surface of the film.

Acknowledgements

We thank CNRS, the Université de Strasbourg (France), Université Paris-Descartes (Paris, France),

Université Pierre et Marie Curie (Paris, France), ICSN, ECE Paris Ecole d'Ingénieurs (France), and Fudan University (Shanghai, China) for funding of this work. We also thank the Université de Strasbourg for the projet "Idex Attractivité 2012" which has also supported one part of this research, as well as the Oversea Study Program of Guangzhou Elite Project (GEP) for the Ph.D. grant of Zhaohui Huo. This work was also supported by Fund of senior visiting professor of Fudan University.

Appendix A. Supplementary data

Supplementary data related to this article can be found at https://doi.org/10.1016/j.electacta.2020.... Content of the supplementary data: experimental details, electrochemistry, EQCM, UV-Vis spectra, XPS, AFM, EIS, and photoelectrochemical responses (Figs. S1–S36).

Author contributions

Laurent Ruhlmann conceived the idea, and initiated the study. He wrote the manuscript with the assistance of all the co-authors. Zhaohui Huo, Shu Yang, Dejin Zang carried out the preparation and characterization of the copolymers as well the EIS and photovoltaic measurements. Yiming Liang has done the measurments in order to check the stability of the fours films. She has also check the photocurrent generation under in front or back illumination and in front illumination with reverse position. Rana Farha and Michel Goldmann have done the AFM measurements. Hualong Xu performed the XPS measurements. Antoine Bonnefont contributed to the analysis of the EIS measurements. He also helped to write the manuscript. This work takes also part of long-term research project on POM photosensitization for solar energy conversion of Guillaume Izzet, and Anna Proust. They carried out the sample preparation and characterization of the hybrid polyoxometalates with the assistance of Edoardo Matricardi. They contributed also to the analysis and the interpretation of the data. All authors discussed the results and commented on the manuscript.

Graphical abstract

Four hybrid polyoxometalate–porphyrin copolymer films were obtained by the electrooxidation of zinc-*β*-octaethylporphyrin or 5,15-ditolylporphyrin in the presence of organosilyl functionalized Keggin-type or Dawson type POMs bearing two pyridyl groups. The electropolymerization process was monitored by EQCM and fully characterized. Their impedance properties (EIS) were studied and their photovoltaic performances were also investigated by photocurrent transient measurements under visible light irradiation. These studies showed a correlation between impedance and photovoltaic performances, the films based on Dawson type POMs and Zn porphyrins giving the best results.

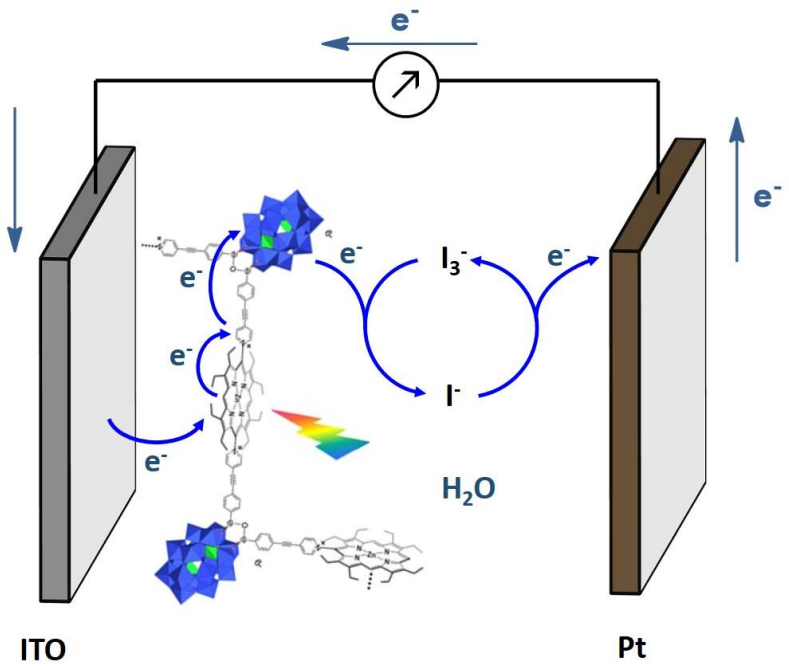

References

[1] D.−L. Long, R. Tsunashima, L. Cronin, Polyoxometalates: building blocks for functional nanoscale systems, Angew. Chem. Int. Edit. 49 (2010) 1736-1758; Polyoxometallate als bausteine für funktionelle nanosysteme, Angew. Chem. Int. Edit. 122 (2010) 1780-1803.

[2] C. Costa-Coquelard, D. Schaming, I. Lampre, L. Ruhlmann, Photocatalytic reduction of Ag_2SO_4 by the Dawson anion α-$[P_2W_{18}O_{62}]^{6-}$ and tetracobalt sandwich complexes, Appl Catal B-Environ. 84 (2008) 835-842.

[3] S. Liu, Z. Tang, Polyoxometalate-Based functional nanostructured films: current progress and future prospects, Nano Today 5 (2010) 267-281.

[4]J. Kang, B. Xu, Z. Peng, X. Zhu, Y. Wei, D.R. Powell, Molecular and polymeric hybrids based on covalently linked polyoxometalates and transition-metal complexes, Angew. Chem. Int. Edit. 44 (2005) 6902-6905.

[5] a) L. Xu, M. Lu, B. Xu, Y. Wei, Z. Peng, D.R. Powell, Towards main-chain-polyoxometalate-containing hybrid polymers: a highly efficient approach to bifunctionalized organoimido derivatives of hexamolybdates, Angew. Chem. Int. Edit. 41 (2002) 4129-4132; Angew. Chem. Int. Ed. 114 (2002) 4303-4306. b) M. Lu, B. Xie, J. Kang, F.C. Chen, Y. Yang, Z. Peng, Synthesis of main-chain polyoxometalate-containing hybrid polymers and their applications in photovoltaic cells, Chem. Mater. 17 (2005) 402-408. c) S. Chakraborty, A. Keightley, V. Dusevich, Y. Wang, Z. Peng, Synthesis and optical properties of a rod-coil diblock copolymer with polyoxometalate clusters covalently attached to the coil block, Chem. Mater. 22 (2010) 3995-4006.

[6] a) B. Xu, M. Lu, J. Kang, D. Wang, J. Brown, Z. Peng, Synthesis and optical properties of conjugated polymers containing polyoxometalate clusters as side-chain pendants, Chem. Mater. 17 (2005) 2841-2851. b) Y. Li, K. Shetye, K. Baral, L. Jin, J.D. Oster, D.M. Zhub, Z. Peng, Main-chain polyoxometalate-containing donor-acceptor conjugated copolymers: synthesis, characterization, morphological studies and applications in single-component photovoltaic cells, RSC Adv. 6 (2016) 29909-29919.

[7] H. Wu, H.K. Yang, W. Wang, Covalently-linked polyoxometalate–polymer hybrids: optimizing synthesis, appealing structures and prospective applications, New J. Chem. 40 (2016) 886-897.

[8] D. Schaming, C. Allain, R. Farha, M. Goldmann, S. Lobstein, A. Giraudeau, B. Hasenknopf, L. Ruhlmann, Synthesis and photocatalytic properties of mixed polyoxometalate-porphyrin copolymers obtained from Anderson-type polyoxomolybdates, Langmuir 26 (2010) 5101-5109.

[9] a) I. Azcarate, I. Ahmed, R. Farha, M. Goldmann, X. Wang, H. Xu, B. Hasenknopf, E. Lacôte, L. Ruhlmann, Synthesis and characterization of conjugated Dawson-type polyoxometalate–porphyrin copolymers, Dalton Trans. 42 (2013) 12688-12698. b) I. Azcarate, Z. Huo, R. Farha, M. Goldmann, H. Xu, B. Hasenknopf, E. Lacôte, L. Ruhlmann, Generation of photocurrent by visible-light irradiation of conjugated Dawson polyoxophosphovanadotungstate–porphyrin copolymers, Chem-Eur. J. 21 (2015) 8271-8280.

[10] Z. Huo, D. Zang, S. Yang, R. Farha, M. Goldmann, B. Hasenknopf, H. Xu, L. Ruhlmann, Synthesis and characterization of Lindqvist-type polyoxometalate–porphyrin copolymers, Electrochim. Acta 179 (2015) 326-335.

[11] B. Matt, C. Coudret, C. Viala, D. Jouvenot, F. Loiseau, G. Izzet, A. Proust, Elaboration of covalently linked polyoxometalates with ruthenium and pyrene chromophores and characterisation of their photophysical properties, Inorg. Chem. 50 (2011) 7761-7768.

[12] B. Matt, J. Fize, J. Moussa, H. Amouri, A. Pereira, V. Artero, G. Izzet, A. Proust, Charge photo-accumulation and photocatalytic hydrogen evolution under visible light at an iridium(III)-photosensitized

polyoxotungstate, Energ. Environ. Sci. 6 (2013) 1504-1508.
[13] R. Salles, B. Abécassis, E. Derat, D. Brouri, A. Bernard, Q. Zhang, A. Proust, C. Desmarets, G. Izzet, Hierarchical self-assembly of polyoxometalate-based organo palladium(II) metallomacrocycles via electrostatic interactions, Inorg. Chem. 59 (2020) 2458-2463.
[14] G. Izzet, A. Macdonell, C. Rinfray, M. Piot, S. Renaudineau, E. Derat, B. Abécassis, C. Afonso, A. Proust, Metal-directed self-assembly of a polyoxometalate-based molecular triangle: using powerful analytical tools to probe the chemical structure of complex supramolecular assemblies, Chem. Eur. J. 21 (2015) 19010-19015.
[15] A. Giraudeau, L. Ruhlmann, L. El Kahef, M. Gross, Electrosynthesis and characterization of symmetrical and unsymmetrical linear porphyrin dimers and their precurso monomers, J. Am. Chem. Soc. 118 (1996) 2969-2979.
[16] L. Ruhlmann, A. Schulz, A. Giraudeau, C. Messerschmidt, J.H. Fuhrhop, A polycationic zinc-5,15-dichlorooctaethylporphyrinate-viologen wire, J. Am. Chem. Soc. 121 (1999) 6664-6667.
[17] D. Schaming, I. Ahmed, J. Hao, V. Alain-Rizzo, R. Farha, M. Goldmann, H. Xu, A. Giraudeau, P. Audebert, L. Ruhlmann, Easy methods for the electropolymerization of porphyrins based on the oxidation of the macrocycles, Electrochim. Acta 56 (2011) 10454-10463.
[18] G. Izzet, A. Macdonell, C. Rinfray, M. Piot, S. Renaudineau, E. Derat, B. Abécassis, C. Afonso, A. Proust, Metal-directedself-assembly of a polyoxometalate-based molecular triangle: using powerful analytical tools to probe the chemical structure of complex supramolecular assemblies, Chem-Eur. J. (2015) 19010-19015.
[19] R. Salles, B. Abécassis, E. Derat, D. Brouri, A. Bernard, Q. Zhang, A. Proust, C. Desmarets, G. Izzet, Hierarchical self-assembly of polyoxometalate-based organo palladium(II) metallomacrocycles via electrostatic interactions, Inorg. Chem. 59 (2020) 2458-2463.
[20] a) V. Carelli, F. Liberatore, A. Casini, S. Tortorella, L. Scipione, B.D. Renzo, On the regio- and stereoselectivity of pyridinyl radical dimerization, New J. Chem. 22 (1998) 999-1004. b) V. Carelli, F. Liberatore, S. Tortorella, B.D. Rienzo, L. Scipione, Structure of the dimers arising from one-electron electrochemical reduction of pyridinium salts 3,5-disubstituted with electron-withdrawing groups, J. Chem. Soc. Pakistan (2002) 542-547.
[21] D. Schaming, S. Marggi-Poullain, I. Ahmed, R. Farha, M. Goldmann, J.-P. Gisselbrechte, L. Ruhlmann, Electrosynthesis and electrochemical properties of porphyrin dimers with pyridinium as bridging spacer, New J. Chem. 35 (2011) 2534-2543.
[22] a) A. Brisach-Wittmeyer, S. Lobstein, M. Gross, A. Giraudeau, Electrochemical reduction of l-(meso-tetraphenylporphyrin)-pyridinium cations, J. Electroanal. Chem. 576 (2005) 129-137. b) D. Schaming, A. Giraudeau, S. Lobstein, R. Farha, M. Goldmann, J.P. Gisselbrecht, L. Ruhlmann, Electrochemical behavior of the tetracationic porphyrins (py)ZnOEP(py)$_4^{4+}$ 4PF_6^- and ZnOEP(py) $_4^{4+}$4Cl^-, J. Electroanal. Chem. 635 (2009) 20-28.
[23] M. El Baraka, J.M. Janot, L. Ruhlmann, A. Giraudeau, M. Deumié, P. Seta, Photoinduced energy and electron transfers in the porphyrin triad (zinc octaethylporphyrin-4,4' bipyridinium-tetraphenylporphyrin)$^{2+}$, 2ClO_4^-), J. Photoch. Photobio. A. 113 (1998) 163-169.
[24] C. Inisan, J.Y. Saillard, R. Guilard, A. Tabard, Y. Le Mest, Electrooxidation of porphyrin free bases: fate of the p-cation radical, New J. Chem. (1998) 823-830.
[25] S. Bruckenstein, M. Shay, Experimental aspects of use of the quartz crystal microbalance in solution, Electrochim. Acta 30 (1985) 1295-1300.
[26] C. Inisan, J.-Y. Saillard, R. Guilard, A. Tabard, Y. Le Mest, Electrooxidation of porphyrin free bases: fate of the p-cation radical, New J. Chem. 22 (1998) 823–830.

[27] a) Q. Wang, J.E. Moser, M. Grätzel, Electrochemical impedance spectroscopic analysis of dye-sensitized solar cells, J. Phys. Chem B 109 (2005) 14945-14953. b) F. Fabregat-Santiago, J. Bisquert, G. Garcia-Belmonte, G. Boschloo, A. Hagfeldt, Influence of electrolyte in transport and recombination in dye-sensitized solar cells studied by impedance spectroscopy, Sol. Energ. Mat. Sol. C. 87 (2005) 117-131. c) M. Adachi, M. Sakamoto, J. Jiu, Y. Ogata, S. Isoda, Determination of parameters of electron transport in dye-sensitized solar cells using electrochemical impedance spectroscopy, J. Phys. Chem. B 110 (2006) 13872-13880.
[28] a) B. Matt, X. Xiang, A.L. Kaledin, N. Han, J. Moussa, H. Amouri, S. Alves, C.L. Hill, T. Lian, D.G. Musaev, G. Izzet, A. Proust, Long lived charge separation in iridium(III)-photosensitized polyoxometalates: synthesis, photophysical and computational studies of organometallic–redox tunable oxide assemblies, Chem. Sci. 4 (2013) 1737-1745. b) C. Bosch-Navarro, B. Matt, G. Izzet, C. Romero-Nieto, K. Dirian, A. Raya, S.I. Molina, A. Proust, D.M. Guldi, C. Martí-Gastaldo, E. Coronado, Charge transfer interactions in self-assembled single walled carbon nanotubes/Dawson–wells polyoxometalate hybrids, Chem. Sci. 5 (2014) 4346-4354.
[29] G. Izzet, F. Volatron, A. Proust, Tailor-made covalent organic-inorganic polyoxometalate hybrids: versatile platforms for the elaboration of functional molecular architectures, Chem. Rec. 17 (2017) 250-266
[30] J.J. Walsh, J. Zhu, A.M. Bond, R.J. Forster, T.E. Keyes, Visible light sensitized photocurrent generation from electrostatically assembled thin films of $[Ru(bpy)_3]^{2+}$ and the polyoxometalate γ*-$[W_{18}O_{54}(SO_4)_2]^{4-}$: optimizing performance in a low electrolyte medium, J. Electroanal. Chem. 706 (2013) 93-101.
[31] J. Zhu, Q. Zeng, S. O'Carroll, A. Bond, T.E. Keyes, R. Forster, Photocurrent generation from thin films of ruthenium metallopolymer: polyoxometalate adducts using visible excitation, Electrochem. Commun. 13 (2011) 899-902.
[32] Y. Wang, C. Hu, Layer-by-layer self-assembly of dye–polyoxometalate multilayer composite films and their fluorescent properties, Thin Solid Films 476 (2005) 84-91.
[33] G. Jin, S.M. Wang, W.L. Chen, C. Qin, Z.M. Su, E.B. Wang, A photovoltaic system composed of a keplerate-type polyoxometalate and a water-soluble poly(p-phenylenevinylene) derivative, J. Mater. Chem. A 1 (2013) 6727-6730.
[34] X. Chen, L.H. Gao, Z.B. Zheng, K.Z. Wang, Photoelectrochemical properties of electrostatically self-assembled multilayer films formed by three bipolar hemicyanines and $H_4SiW_{12}O_{40}$, Mater. Res. Bull. 48 (2013) 595-602.
[35] L.H. Gao, Q.L. Sun, J.M. Qi, X.Y. Lin, K.Z. Wang, Enhanced photocurrent generation from an electrostatically self-assembled film of sandwich-type tetracadmium(II) tungstophosphorate/hemicyanine, electrochim. Acta 92 (2013) 236-242.
[36] L. Gao, Q. Sun, K. Wang, Photoelectrochemical properties of a series of electrostatically self-assembled films based on sandwich-type polyoxometalates and a bichromophore hemicyanine dye, J. Colloid Interf. Sci. 393 (2013) 92-96.
[37] L. Gao, Q. Sun, X. Lin, J. Qi, K. Wang, Photoelectrochemical properties of three inorganic/organic hybrid films formed from sandwich-type tetrazinc(II) tungstophosphorate and hemicyanines with varied alkyl chain lengths, Colloid. Surface. A 423 (2013) 162-169.
[38] Y. Yang, L. Xu, F. Li, X. Du, Z. Sun, Enhanced photovoltaic response by incorporating polyoxometalate into a phthalocyanine-sensitized electrode, J. Mater. Chem. 20 (2010) 10835-10840.
[39] Z. Sun, S. Fang, F. Li, L. Xu, Y. Hu, J. Ren, Enhanced photovoltaic performance of copper phthalocyanine by incorporation of polyoxometalate, J. Photoch. Photobio. A. 252 (2013) 25-30.
[40] I. Ahmed, R. Farha, Z. Huo, C. Allain, X. Wang, H. Xu, M. Goldmann, B. Hasenknopf, L. Ruhlmann, Porphyrin–polyoxometalate hybrids connected via a tris-alkoxo linker for the generation of photocurrent, Electrochim. Acta 110 (2013) 726-734.

[41] I. Ahmed, R. Farha, M. Goldmann, L. Ruhlmann, A molecular photovoltaic system based on dawson type polyoxometalate and porphyrin formed by layer-by-layer self assembly, Chem. Commun. 49 (2013) 496-498.
[42] a) J.J. Walsh, C.T. Mallon, A.M. Bond, T.E. Keyes, R.J. Forster, Enhanced photocurrent production from thin films of Ru(II) metallopolymer/dawson polyoxotungstate adducts under visible irradiation, Chem. Commun. 48 (2012) 3593-3595. b) S. Gao, R. Cao, C. Yang, Dye–polyoxometalate composite films: self-assembly, thermal and photochemical properties, J. Colloid Interf. Sci. 324 (2008) 156-166. c) J.J. Walsh, A.M. Bond, R.J. Forster, T.E. Keyes, Hybrid polyoxometalate materials for photo(electro-) chemical applications, Coordin. Chem. Rev. 306 (2016) 217-234.